INTERNATIONAL JOURNAL OF AVIATION SCIENCE AND TECHNOLOGY
IJAST
www.ijast.org

International Journal of Aviation Science and Technology

Volume 4, Issue 1, JUNE 2023

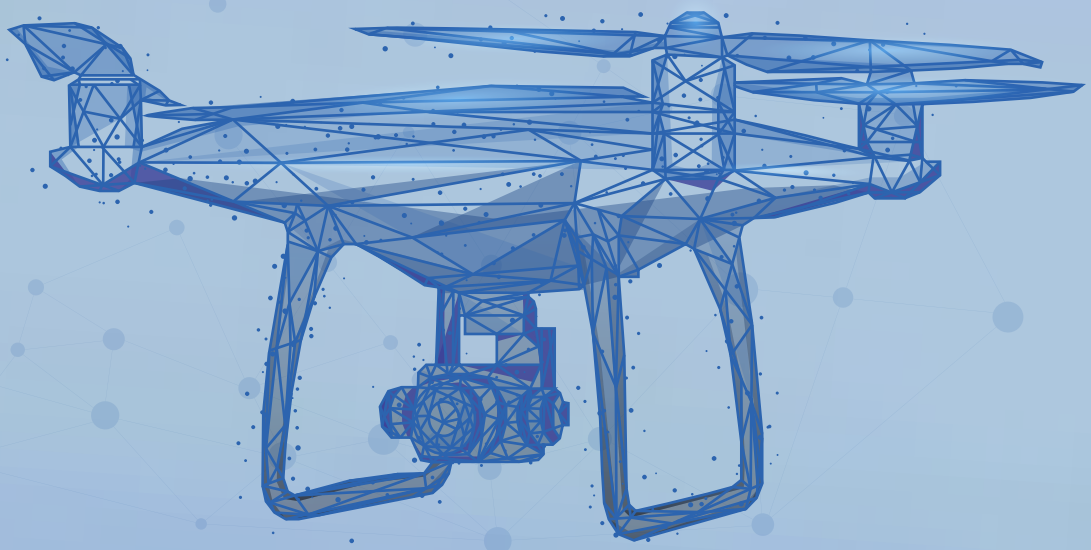

e-ISSN: 2687-525X

INTERNATIONAL SUSTAINABLE AVIATION AND ENERGY RESEARCH SOCIETY
SARES

www.sares.org

International Journal of Aviation Science and Technology

Publisher	:	SARES International Sustainable Aviation and Energy Research Society
Licence holder	:	Prof. Dr. T. Hikmet Karakoç (President, SARES)
Address	:	Research and Application Center of Civil Aviation, Research Centers Building, Eskisehir Technical University, Eskisehir, Turkiye

e-ISSN	:	2687-525X
DOI	:	10.23890/IJAST
web	:	www.ijast.org
submission	:	DergiPark-IJAST
e-mail	:	ijast@sares.org
Copyright	:	SARES Society

IJAST is published with the contribution of "Research and Application Center of Civil Aviation, Eskisehir Technical University"

International Journal of Aviation Science and Technology

Index

International Journal of Aviation Science and Technology

Research Article

Electric Aircraft Battery Performance: Examining Full Discharge Under Two Conditions

Denner Cunha[1], Brooke Wheeler[2]*, Isaac Silver[3], Gaspar Andre[4]

[1] *Florida Institute of Technology: Melbourne, Florida, US*
dcunha2022@my.fit.edu - 0000-0002-4366-2966

[2] *Florida Institute of Technology: Melbourne, Florida, US*
bwheeler@fit.edu - 0000-0001-5507-729X

[3] *Energy Management Aerospace: Satellite Beach, Florida, US*
isaac@energymanagementaero.com - 0000-0003-0042-7605

[4] *Florida Institute of Technology: Melbourne, Florida, US*
gandre2020@my.fit.edu - 0000-0002-1786-2139

Abstract

The understanding of battery performance, particularly over the full course of discharge and over battery life is critical to allow pilots to maintain safety in electric aviation. In this study, an electric aircraft powered by two Lithium-Ion battery packs is used as a test article. The objectives of the current study are to build on previous work by conducting two full tests discharging both battery packs from a 100% charge. This allows examination of the battery performance a) under a constant power output and b) with periodic tests of the maximum power available. In addition to state of charge (SOC), remaining flight time, battery temperature, and motor power, this study presents data on motor RPM, torque, voltage, current, battery internal resistance, and available energy. The data on motor power indicates that the available maximum power decreases with lower SOCs when the throttle settings are varied; however, at lower power settings, such as an optimum cruise at 27 kW, the motor power remains constant and as expected during discharge. Also, the constant power setting illustrates that there are inflection points in physical battery characteristics. These results confirm that electric aircraft performance changes during a flight are different than what a pilot expects from a gasoline-powered aircraft. The longer the aircraft flies at different throttle settings, the faster the batteries discharge; the discharge curve is nonlinear. Thus, a piston-trained pilot's expectation for an aircraft's performance later in a flight will not match an electric aircraft.

Keywords

Electric aircraft
Battery
State of health (SOH)
State of charge (SOC)
Performance
Available power

Time Scale of Article

Received 01 December 2022
Revised until 15 March 2023
Accepted 14 May 2023
Online date 28 June 2023

1. Introduction

As aviation moves towards sustainability, one of the technological advances already available is electric aircraft, which are propelled by battery-powered electric motors. When paired with sustainable energy sources, such as solar power, electric aircraft would have the potential to drastically reduce both carbon dioxide emissions as well as other by-products of combustion (Neuman, 2016). An added benefit of fully electric aircraft is a substantial reduction in noise pollution.

*: Corresponding Author Brooke Wheeler, bwheeler@fit.edu
DOI: 10.23890/IJAST.vm04is01.0101

Lithium-ion batteries (LIBs) are the dominant chemistry used commercially, although other technologies are being studied to improve aviation battery options (Dornbusch et al., 2022). The energy typically stored in batteries has not reached the ideal density of approximately 500 Wh/kg; instead, 150 to 250 Wh/kg is more commonly available (Tom et al., 2021). Battery development for electric aircraft is ongoing with goals of efficiency, improved range, and performance.

Furthermore, LIBs have exact operational requirements to maintain both performance and battery life including battery temperature maxima and minima and safe voltages (Li et al., 2022). According to recent studies (e.g., Hashem et al., 2020, Tariq et al., 2018), a Battery Management System (BMS) entails monitoring the battery's performance through key indicators such as state of health (SOH), remaining useful life (RUL), and state of charge (SOC).

Essentially, the SOH is meant to assess the aging degree of LIBs, resulting from the difference between the available energy that a battery can currently deliver and its capacity at the beginning of its operational life. According to (Li et al., 2022), a SOH analysis focuses primarily on three health indicators, namely fade capacity, internal resistance, and voltage, enabling an estimation and monitoring of the battery's behavior and age. The RUL, in turn, is predicted as the remaining operational time for a battery before it is decommissioned. Parameters such as lithium concentration available to generate the electrical charge, kinetic energy within the cell, and charge transfer are often used to predict the RUL (Elmahallawy et al., 2022).

The European Aviation Safety Agency (EASA) already has certified electric aircraft in operation. A minimum flight time reserve of 10 minutes in battery charge is required for operations at one airport under EASA regulations (EASA, 2022). Electric aircraft are also operated as experimental aircraft and are likely to be certified by other aviation organizations in the future. This shift in aviation towards electric propulsion requires research on battery management and performance.

As flight time for an electric vehicle is predicated on the ability of the battery to provide the observed power required, this study looked at the max power available at a given SOC as well as the behavior of the battery during a continuous discharge to a low SOC.

The SOC in Battery Management

The SOC is a popular metric for estimating how much electrical energy is still present in a battery. It is defined as the percentage ratio between the available charge at any given time and the total battery capacity (Rozas, et al., 2021). According to (Xu et al., 2020), the estimation of SOC is intended to accomplish a twofold battery performance goal. Firstly, SOC indicates the remaining amount of energy a battery has when compared with the energy it had when fully charged. Secondly, SOC provides the operator with an estimation of how long a battery will last before needing to be recharged. The accuracy of SOC estimation is of crucial importance to the operational safety of a battery pack (Xu et al., 2021).

One of the battery management issues is to determine the lowest SOC below which a battery cannot be safely operated. In their study, (Isikveren et al., 2017) contended that given the fact that a battery is an electrochemical structure, it should not be operated below 20% of its SOC to avoid damage to the electrodes, affecting thereby the battery's operational life.

Testing Battery Characteristics During Discharge

An initial exploration of the battery characteristics during discharge was previously conducted. The SOC, battery temperature, and available motor power were monitored after a regular test flight in an electric aircraft, discharging the batteries from the remaining 53% charge. Battery cell temperatures increased over the course of the test run (maximum 39°C); however, the temperature management was sufficient until a low state of charge. The output for SOC and remaining flight time decreased concurrently, with the exceptions of the first few minutes of the test and very low SOCs. The decrease in maximum available engine power in the last 30% of battery SOC was concerning because it suggested that the expected power may not be available at lower battery SOC, which is when an emergency go-around might be needed.

We wanted to replicate the initial discharge test under controlled conditions. The objectives of the current study were to build on a previous study by conducting two full tests discharging both battery packs from a full (100%) charge. This allowed examination of the battery performance a) under a constant power output and b) with periodic tests of the maximum power available. In addition to SOC, remaining flight time, battery temperature, and motor power, this study presents data on motor RPM, torque, voltage, current, battery internal resistance, and available energy. Furthering our understanding of battery performance, particularly over the full course of discharge and over battery life, is critical to allow pilots to interpret this information during aeronautical decision-making and thus to maintaining safety in electric aviation.

2. Method

The test article was a single-engine electric aircraft powered by two liquid-cooled battery packs. The battery

packs were comprised of cylindrical Lithium Ion cells, with a hybrid matrix of NiMgCo (Nickel Manganese Cobalt). Power is produced by an AC axial-flux motor, which drives a three-blade fixed-pitch propeller mounted directly on the rotor. At full charge (100%), the motor can generate a peak power of 69 kW. The powertrain system also includes an inverter (a.k.a. motor controller), which adjusts the current from the batteries and converts DC to three-phase AC. The test article is certified in Europe by EASA as a light-sport aeroplane (LSA), but not certified in the US, where it operates as an experimental aircraft for research and development purposes.

Because of mandated fuel/power reserves and safety, electric aircraft battery performance cannot be tested to 0% during flight. However, the engine can be run until the batteries fully discharge on the ramp. To execute the experimental runs, the aircraft was tied down by the main landing gear, and the wings were detached from the fuselage.

Two test cases were performed, both starting at 100% battery SOC and completed when 0% was achieved. In Test Case 1, Maximum Take Off Power (MTOP) was initiated, and the throttle setting was gradually reduced to idle. Next, starting when SOC was approximately 75%, for every 10% decrease in battery SOC, the throttle setting was increased to full. In Test Case 2, a constant motor power of 27 kW was maintained during the discharge. This value represents an optimum cruise setting at level flight or a typical cruise power with two passengers onboard, according to the test pilot's experience.

All data output from the aircraft was collected through a flight data recorder at a frequency of 5 Hz. Table 1 summarizes the parameters and units used for the data analysis.

Table 1. Parameters provided by the flight data recorder that were used for the data analysis

Parameter	Unit
Motor Power	kW
Motor RPM	Rpm
Requested Torque	% max. torque
Motor Temperature	°C
Current (Battery Packs 1 & 2)	A
Voltage (Battery Packs 1 & 2)	V
Available Energy (Battery Packs 1 & 2)	kWh
SOC (Battery Packs 1 & 2)	%
SOH (Battery Packs 1 & 2)	%
Average Cells Temp. (Battery Packs 1 & 2)	°C
Remaining Flight Time	min
Elapsed Time	ms

Additionally, other parameters were calculated from the flight recorder data output. In physics, power is the rate at which a force does work and was calculated according to Eq 1 (Tipler and Mosca, 2008).

$$P = F * v \quad (1)$$

P : power (W)

F : force acting on the particle (N)

v : instantaneous velocity (m/s)

Since electric motors involve a rotating shaft, as in a reciprocating engine, power can be related to the rotational properties of torque and angular speed (Eq 2).

$$P = \tau * \omega \therefore P_{Motor} = Q_{Motor} * RPM * \frac{2\pi}{60} \quad (2)$$

τ : torque acting on the particle (N.m)

ω : instantaneous angular velocity (rad/s)

P_{Motor} : motor power (W)

Q_{Motor} : motor torque output (N.m)

RPM : motor revolutions per minute (rpm)

Electric power is the rate at which electrical energy is transferred by an electric circuit. For a resistor in a DC circuit, the power was calculated by Eq 3 (Tipler and Mosca, 2008).

$$P_{Bat} = V_{Bat} * I_{Sys} \quad (3)$$

P_{Bat} : power available from the battery pack (W)

V_{Bat} : battery pack voltage (V)

I_{Sys} : current required by the motor-controller (A)

Finally, battery internal resistance was calculated using Eq 4.

$$R_{Bat} = \frac{V_{Bat}}{I_{Sys}} \quad (4)$$

R_{Bat} : battery internal resistance (Ω)

3. Results and Discussion

Regular flight tests have indicated battery SOC and motor performance decreasing as expected during the battery discharge. These findings confirmed the initial test run previously conducted for the last 53% SOC. This experiment used two different throttle settings to fully discharge the batteries from 100% SOC to 0%; the battery packs were at a SOH of 88% for this study. The discharge was accomplished in approximately 53 minutes in both test cases.

The basic battery characteristics data are presented in Table 2 for Test Case 1 and Table 3 for Test Case 2. These results will be discussed and analyzed throughout this section, along with additional data.

Fig. 1 shows the motor power over the course of the battery's discharge. In Test Case 1, the throttle was advanced to full and was gradually reduced to idle. Next, when SOC was approximately 75%, full throttle was set

at approximately every 10% decrease in the battery SOC. In Test Case 2, the pilot kept a constant cruise power setting of 27 kW

Table 2. Test case 1: data for MTOP and test of maximum power after each 10% decrease ın SOC.

SOC [%]	Motor Power [kW]	Motor RPM [rpm]	Voltage per battery pack [V]	Current per battery pack [A]
100	67	2377	399	93.4
75	65	2325	348	93.5
70	64	2294	343	93.8
60	63	2330	333	96.3
50	63	2343	323	98.9
40	62	2309	315	99.8
30	62	2282	311	101.9
22	61	2226	305	101.5
15	53	2162	301	90.2
10	57	2232	294	101.7

Note that in Test Case 1, while the full engine power of approximately 65 kW was achievable for most of the test, as the SOC of the battery decreased, so did the maximum motor power. After battery SOC dropped to 45%, the reduction in maximum power was above 10%. Below 15% SOC, the power generation became unpredictable, and the maximum power was substantially lower than that listed for the motor. Thus, at lower SOCs, the motor does not produce the maximum rated power at a full throttle setting. At a SOC of approximately 6%, the batteries lost the ability to supply power, even though 0% SOC had not been achieved yet.

Table 3. Test case 2: data for constant 27 kW power discharge.

SOC [%]	Motor Power [kW]	Motor RPM [rpm]	Voltage per battery pack [V]	Current per battery pack [A]
100	27	1800	385	37.4
75	27	1800	360	39.1
70	27	1800	356	39.6
60	27	1800	348	40.5
50	27	1800	339	41.6
40	27	1800	331	42.5
30	27	1800	323	44
22	27	1800	318	44.4
15	27	1800	313	45.1
10	27	1800	309	45.8

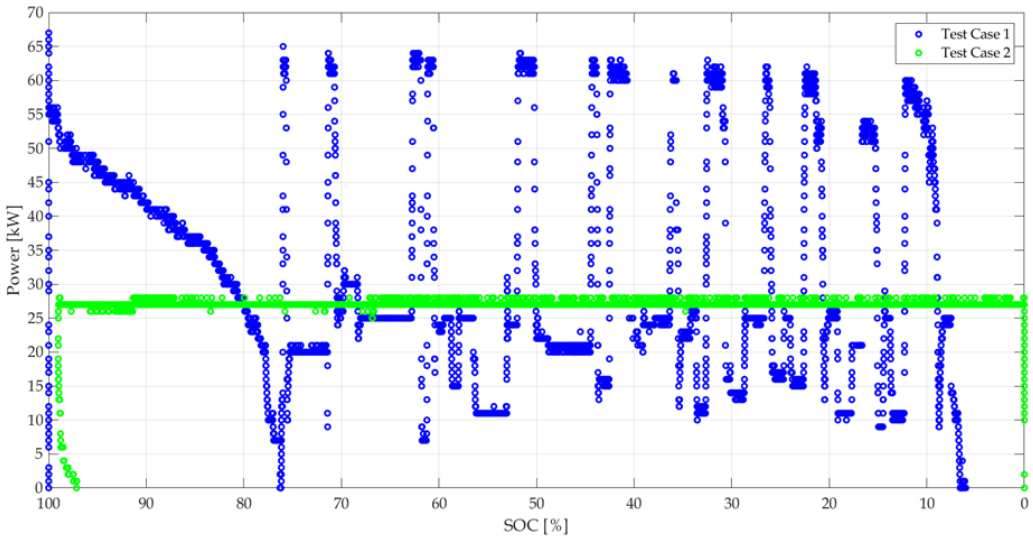

Fig. 1. Motor Power over the course of the battery's discharge

The pilot advanced the throttle to full at approximately 10% SOC intervals. Full throttle could not be continuously maintained because of the motor high temperature limits. The battery temperature remained within limits for the test. At no time did the motor or battery exceed the specified maximum temperature limits.

In Test Case 2, on the other hand, the battery's ability to supply power was consistent throughout the discharge. This constant power output was as expected and indicates that at intermediate power settings the batteries provided the expected power across the entire discharge run.

Through motor power and RPM (Fig. 2), torque output was calculated using Eq 2. Next, the values were normalized and compared with the requested torque extracted from the data logger, as shown in Fig. 3.

As with any mechanical system, electrical motors also present a loss in torque during the conversion of

electrical energy into mechanical energy. Thus, as expected, the data in Fig 3 was concentrated above the red diagonal line, indicating that the torque requested by the motor controller was greater than the torque output produced by the motor. The same relationship can be observed between the motor power and the power available (Fig. 4) from the battery pack, which was calculated via Eq 3. After eliminating the outliers, a mean value of approximately 3% in loss of power was found.

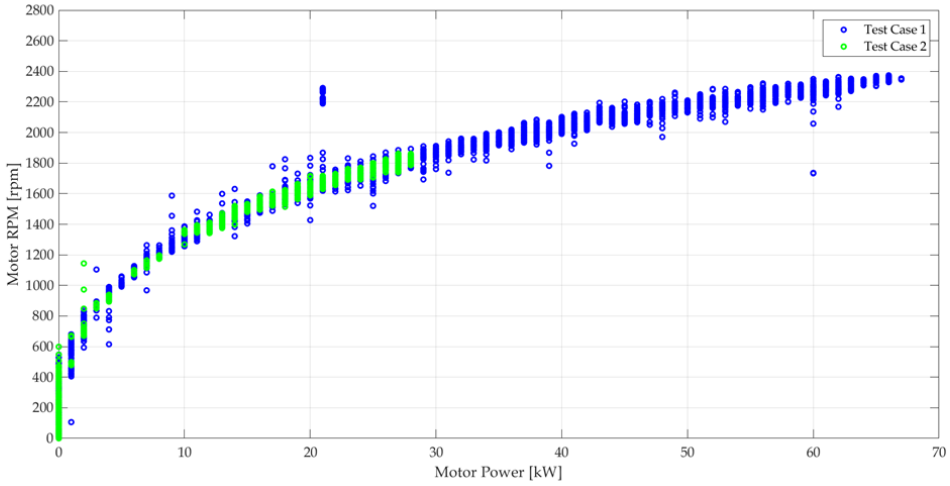

Fig. 2. Motor RPM vs. Motor Power

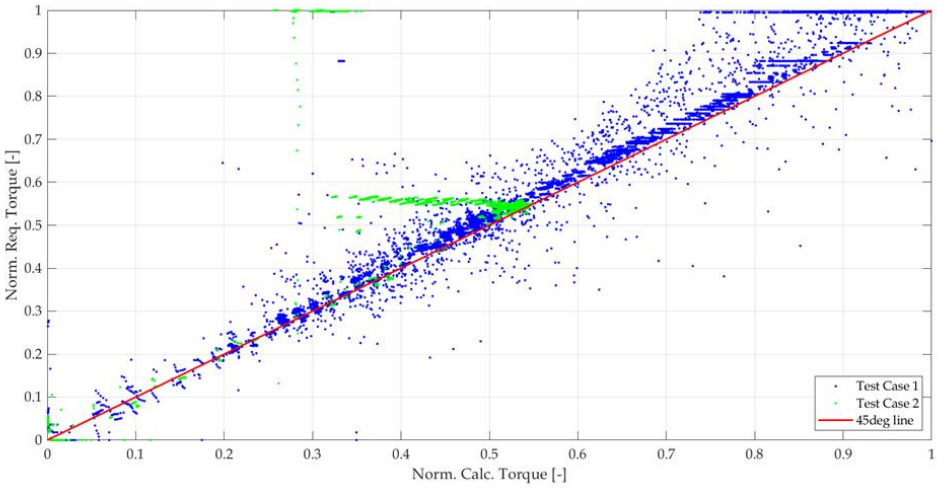

Fig. 3. Normalized Requested Torque vs. Normalized Calculated Torque

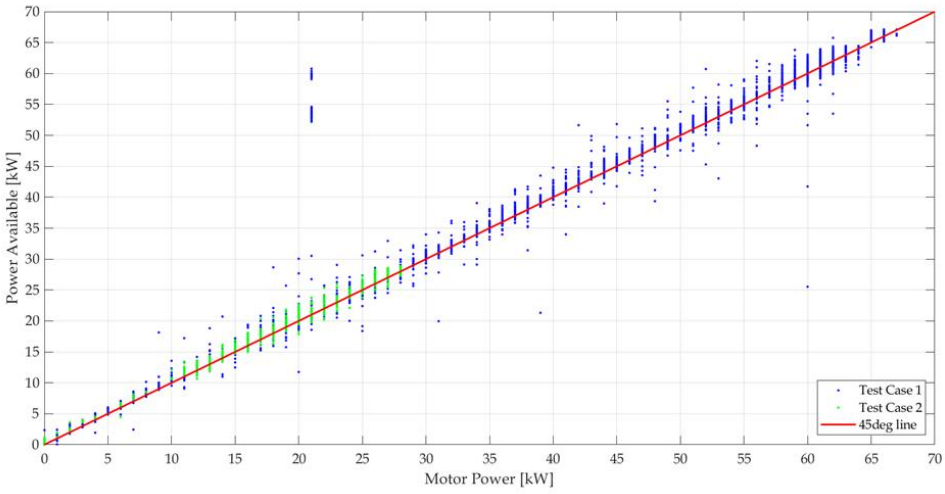

Fig. 4. Power Available vs. Motor Power

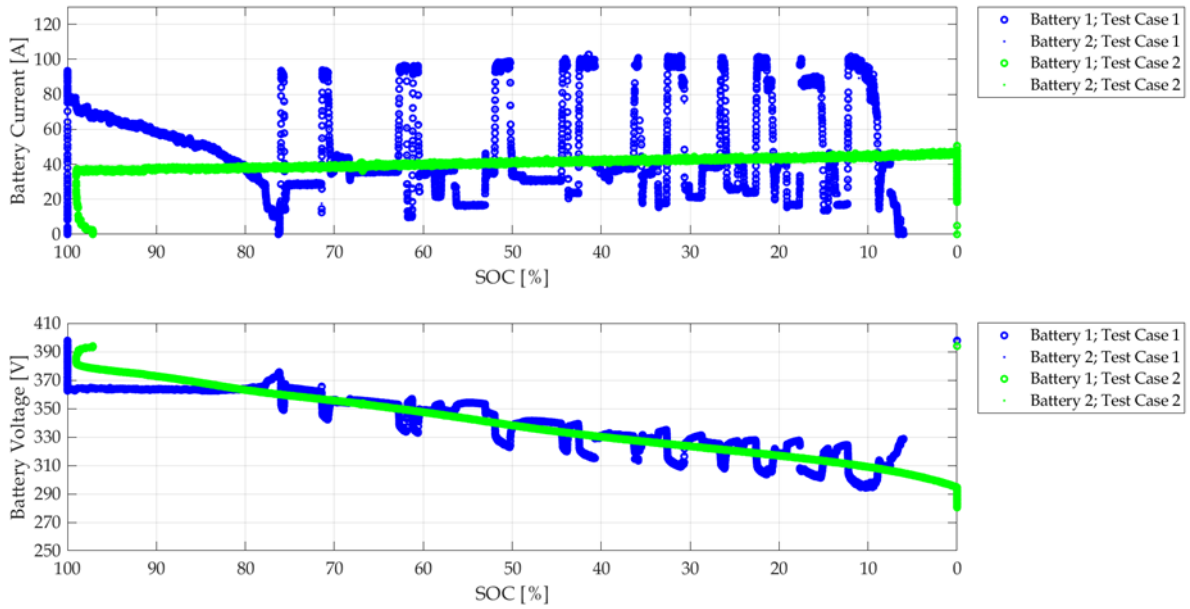

Fig. 5. Current and voltage provided by the battery packs over the course of the discharge

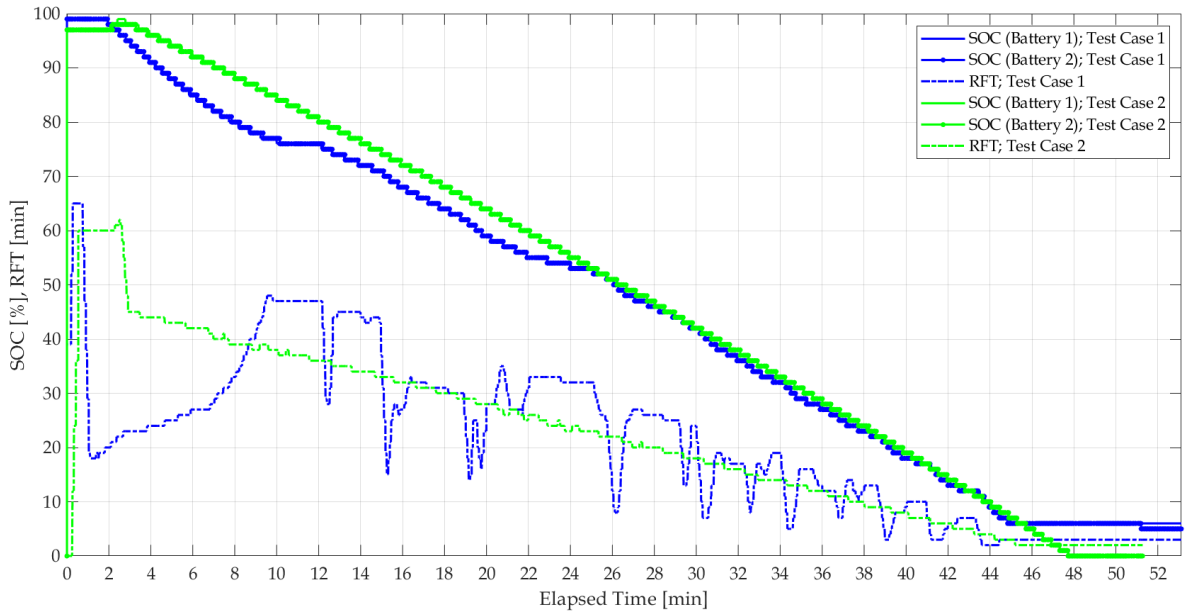

Fig. 6. State of Charge and Remaining Flight Time

Fig. 5 shows the voltage and current readings obtained during the discharge of the batteries. The data for batteries 1 and 2 are superimposed on each other, indicating their comparable performance. This supports the reliability of the battery packs as both batteries behaved similarly. As can be noted, the voltage of the batteries drops along the discharge curve. Therefore, to deliver power to the motor, the motor controller requires a higher current (see Eq 3). This behavior is evident in Test Case 2 and can be noted by comparing each peak of battery current in Test Case 1 (see Table 2). Note that at higher SOCs (above 45%), when maximum power is requested, the current output is maintained, resulting in a flat peak at the maximum power achieved. However, as SOC decreases, the current drops off almost immediately, creating a curved decline in current. This is particularly evident at 10% SOC.

Fig. 6 depicts both remaining flight time (RFT) and state of charge (SOC), which is equivalent between both battery packs. Both parameters are plotted on the same scale.

As expected, both curves decrease over the course of the test runs. In Test Case 2, SOC remains quite linear along the discharge due to the constant motor power. However, in both test cases, initial estimates of flight time in the first few minutes are severely low. The RFT estimated during the final seven minutes in Test Case 1

remains constant, as does the SOC, until no battery power is delivered. The dips in the RFT in Test Case 1 occur during the maximum engine power tests. SOC and RFT did not agree at various times, creating a confounding decision-making environment for pilots. In a traditional fuel-burning aircraft, the endurance calculation is a well-known procedure, and it is based on the amount of fuel contained in the tanks. For an electric vehicle, the overall energy available and energy consumption are less trivial to assess, and new metrics never used before may be required to accurately depict the energy state (Verberne et al., 2022).

Both batteries and motor temperatures were monitored until the very end of the test cases. Fig. 7 shows that the motor temperature increased substantially in the first 12 minutes, but then stabilized at approximately 75°C. Both batteries had approximately the same average temperature. The thermal management system worked well overall, but in the final minutes, the battery temperature increased, reaching 48°C as battery SOC approached 0. This temperature was nine degrees higher than the maximum battery cell temperature (39°C) reached during the previous study; this difference is likely due in part to this study conducting a discharge starting from 100%, and the higher SOH of the batteries during the prior study.

Battery internal resistance depends on the battery age, the battery temperature, and the battery SOC (Favier et al., 2021). This parameter was calculated through Eq 4 and is graphically presented in Fig. 8. Data from Test Case 2 shows that the internal resistance decreases when battery temperature increases. The peaks observed in Test Case 1 are related to the voltage drops when maximum discharge power was required.

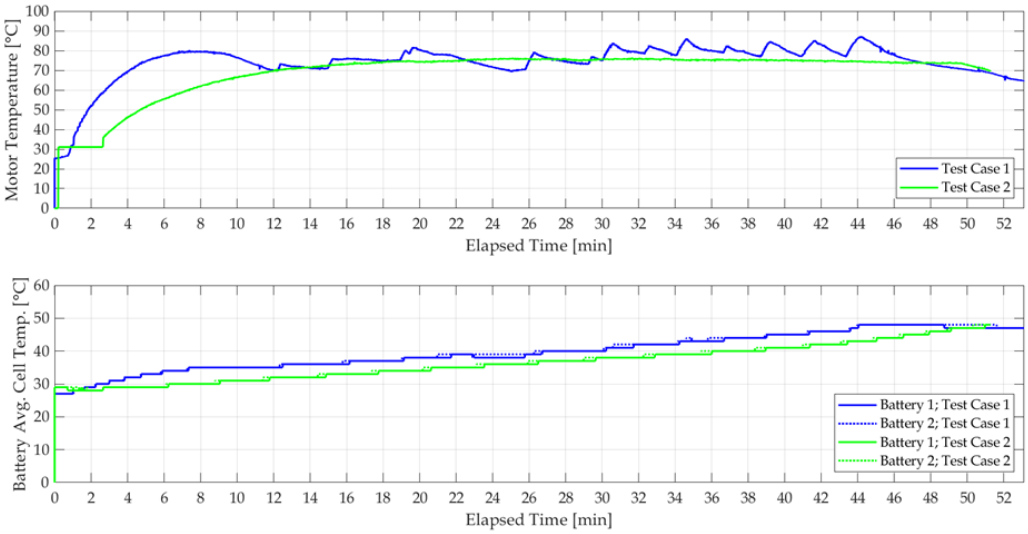

Fig. 7. Motor and Battery Cells Average Temperatures

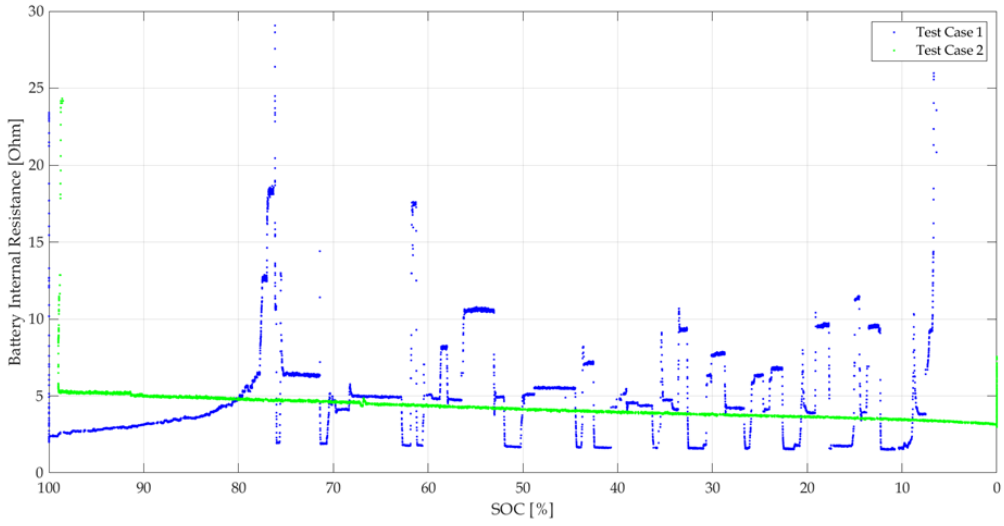

Fig. 8. Battery Internal Resistance varying with temperature, SOC, and voltage drops. Battery Internal Resistance varying with temperature, SOC, and voltage drops

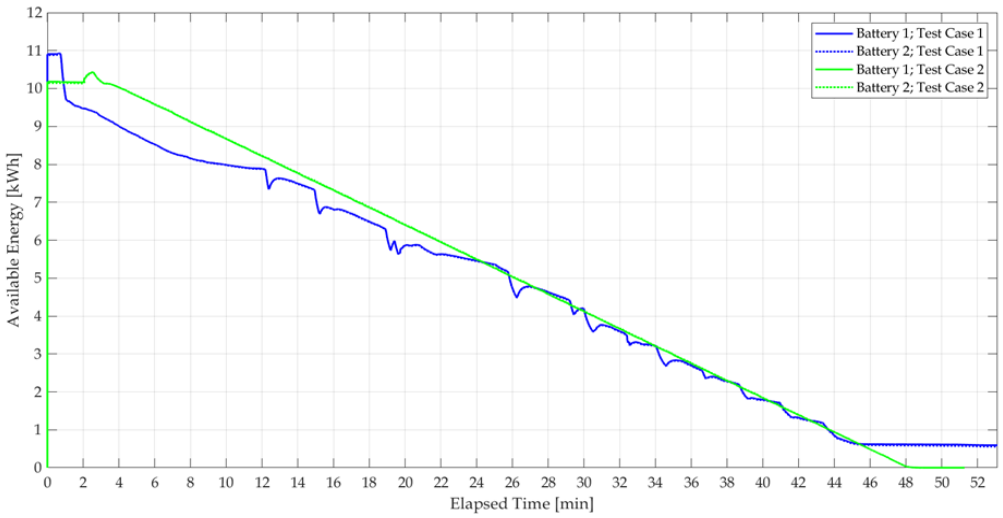

Fig. 9. Available energy for each battery pack over the course of the discharge

Finally, Fig. 9 presents the available energy for each battery pack over the course of the discharge. This parameter indicates the amount of energy that the battery manages to supply the motor controller at a given power setting, considering all losses. Test Case 1 demonstrates that as more power is requested during the discharge cycle, less energy has become available

4. Conclusions

The data on motor power indicates that the available maximum power decreases with lower SOCs when the throttle settings are varied (e.g., Test Case 1); however, at lower power settings, such as an optimum cruise at 27 kW, the motor power remained constant and as expected during discharge. In Test Case 2, the constant power setting illustrated that there are inflection points in physical battery characteristics. As temperature increases and SOC decreases, the voltage also decreases. The changes in battery characteristics are not linear, however. These test runs verified that as SOC decreases below 45% and with higher temperatures, there is more resistance in the batteries.

Pilots cannot continuously interact with the battery information display. This means that an electric aircraft may move into a state of decreased performance with no warning to the pilot. Pilots will need to be aware of lower maximum power availability at low SOCs, especially in the event of an emergency go-around. The study provided invaluable insight into a battery's remaining operational life to aid pilots' decision-making for safer and optimized flight planning with respect to electric aircraft.

For a given aircraft, the battery performance and characteristics should be determined in order to better educate pilots on aircraft performance. One of the advantages of battery-powered aircraft is that as new battery chemistries and/or technologies become available, the batteries in an electric aircraft can be switched out. However, a characterization of the battery performance with the airframe is crucial for understanding performance with what effectively amounts to a new form of fuel.

These results confirm that electric aircraft performance changes during a flight are different than what a pilot expects from a gasoline-powered aircraft. In a piston aircraft, the rated maximum power available at full throttle remains constant throughout the flight, while the weight of the aircraft is decreasing. This results in increased performance near the end of a flight because of the decreased weight due to the burned fuel. However, in the test article, and presumably other battery-powered aircraft, the weight remained constant, and there was lower performance (i.e., motor power) at the lower SOC near the end of the test runs. The longer the aircraft flies at different throttle settings, the more difficult it is for the operator to predict the battery states and, therefore, the usable energy; the discharge curve is nonlinear. Thus, a piston-trained pilot's expectation for an aircraft's performance later in a flight will not match an electric aircraft.

The basic battery characteristics data are presented in Table 2 for Test Case 1 and Table 3 for Test Case 2. These results will be discussed and analyzed throughout this section, along with additional data.

Nomenclature

AC : Alternate Current

BMS : Battery Management System

DC : Direct Current

EASA : European Aviation Safety Agency

LIBs : Lithium-Ion Batteries

LSA : Light-Sport Aeroplane

MTOP : Maximum Take Off Power

NiMgCo : Nickel Manganese Cobalt

RPM : Revolutions per Minute

RFT : Remaining Flight Time

RUL : Remaining Useful Life

SOC : State of Charge

SOH : State of Health

US : United States

CRediT Author Statement

Denner Cunha: Software, Formal analysis, Data Curation, Visualization, Writing- Original Draft, Writing- Review & Editing. **Brooke Wheeler**: Conceptualization, Coordinated Research Efforts, Resources, Writing- Original Draft, Writing- Review & Editing, Supervision, Project Administration, Funding Acquisition. **Isaac Silver**: Conceptualization, Methodology, Investigation, Resources, Writing- Original Draft, Writing- Review & Editing, Project Administration, Funding Acquisition. **Gaspar Andre**: Writing- Original Draft, Writing- Review & Editing.

References

Dornbusch, D., Viggiano, R. P., Wu, J., Lin, Y., Connell, J., and Lvovich, V., 2022. Design Considerations for Practical Li-S Battery Components for Electric Aviation. ECS Meeting Abstracts, Volume MA2022-01, A01: New Approaches and Advances in Electrochemical Energy Systems. Abstr. MA2022-01 133.

Elmahallawy, M., Elfouly, T., Alouani, A., and Massoud, A. M., 2022. A Comprehensive Review of Lithium-Ion Batteries Modeling, and State of Health and Remaining Useful Lifetime Prediction. IEEE Access, 9(2022), vol. 10, pp. 119040-119070, 2022, doi: 10.1109/ACCESS.2022.3221137.

European Union. Easy Access Rules for Air Operations (Regulation (EU) No 965/2012), ED Decision 2022/005/R, AMC1 NCO.OP.125. Page 1837(2022). https://www.easa.europa.eu/downloads/20342/en.

Favier, A., Roberts, S., Esfeld, J., and Uchida, J., 2021. Things Flight Testers Should Know About Batteries for Electric Propulsion. 52nd SFTE International Symposium. St. Louis, MO, 2021.

Hashem, S. R., Roja, E., Nazari, A., Aliniagerdroudbari, H., Alhadri, M., Zakri, W., Mohammed, A.H., Mahajan, A., and Farhad, S., 2020. A Fast Diagnosis Methodology for Typical Faults of a Lithium-Ion Battery in Electric and Hybrid Electric Aircraft. Journal of Electrochemical Energy Conversion and Storage. 17(2020), 011011-1. https://doi-org.portal.lib.fit.edu/10.1115/1.4044956.

Isikveren, A. T. , Pornet, C., Vratny, P. C., and Schmidt, M., 2017. Optimization of Commercial Aircraft Using Battery-Based Voltaic-Joule/Brayton Propulsion. Journal of Aircraft, vol. 54, p.p. 246-261, 2017, doi: 10.2514/1.C033885, https://doi.org/10.2514/1.C033885.

Li, R., Hong, J., Zhang, H., and Chen, X., 2022. Data-driven battery state of health estimation based on interval capacity for real-world electric vehicles. Energy, vol. 257, 2022, 124771, ISSN 0360-5442, https://doi.org/10.1016/j.energy.2022.124771.

Neuman, T., 2016. Fly the Electric Skies. IEEE Spectrum 53(2016), 6, 44-48.

Rozas, H., Troncoso-Kurtovic, D., Ley, C. P., and Orchard, M. E. (2021). Lithium-ion battery State-of-Latent-Energy (SoLE): A fresh new look to the problem of energy autonomy prognostics in storage systems. Journal of Energy Storage, 40(2021), 102735, https://doi.org/10.1016/j.est.2021.102735.

Tariq, M., Ali, I. Maswood, A. I., Gajanayake, C. J., and Gupta, A. K. (2018). Modeling and Integration of a Lithium-Ion Battery Energy Storage System with the More Electric Aircraft 270 V DC Power Distribution Architecture. IEEE Access, 6(2018), 41785-41802.

Tipler, P. and Mosca, G., 2008. Physics for Scientists and Engineers, 6th ed. W.H. Freeman and Company, New York, NY.

Tom, L., Khowja, M., Vakil, G., and Gerada, C., 2021. Commercial Aircraft Electrification—Current State and Future Scope. Energies. 14(2021), 8381. https://doi.org/10.3390/en14248381.

Verberne, J., Beedie, S., Harris, C., Justin, C., and Mavris, D., 2022. Development of a Simulation Environment to Track Key Metrics to Support Trajectory Energy Management of Electric Aircraft. AIAA Aviation 2022 Forum, 2022. Chicago, Illinois. (Published). https://doi.org/10.2514/6.2022-3255.

Xu, Z., Wang , J., Fan, Q., Lund, P. D., and Hong, J., 2020. Improving the state of charge estimation of reused lithium-ion batteries by abating hysteresis using machine learning technique. Journal of Energy Storage, vol. 32, 2020, 101678, ISSN 2352-152X, https://doi.org/10.1016/j.est.2020.101678.

International Journal of Aviation Science and Technology

Research Article

Architecture of Stratosphere Rocket for Cubesats

Alper Şanlı[1]*, Tuncay Yunus Erkeç[2], Melih Beceren[3], Mehmet Furkan Kemallı[4]

[1] National Defence University, Institute of Atatürk Strategic Studies and Graduate, Istanbul, Turkey
alpersanli16@gmail.com - 0000-0002-4338-7685

[2] National Defence University, Institute of Atatürk Strategic Studies and Graduate, Istanbul, Turkey
tuncayyunus@gmail.com - 0000-0003-3357-0985

[3] National Defence University, Institute of Atatürk Strategic Studies and Graduate, Istanbul, Turkey
melihbeceren@gmail.com - 0000-0002-8728-0812

[4] Trendyol Group, System Engineer, Ankara, Turkey
kemallifurkan@gmail.com - 0000-0003-2052-3397

Abstract

Cubesat missions are evolving, and because of their high efficiency, they are becoming more common. Cubesats can go to space more easily because of their compact size. Launch vehicles provide great opportunity for us to reach space and high altitudes of the atmosphere. Today, cubesats are launched to high altitudes for experimental purposes with the help of launch vehicles. In this investigation, a novel launch vehicle was created to match the cubesat's specifications. A stable launch vehicle that can take a cubesat the size of 3U to the stratospheric layer has undergone its first design and examination. Flight simulations were carried out by researching the design stages considered in the launch vehicle. The first design of the launch vehicle suitable for the desired task was made and the altitude, stability and drag analyzes that this design could reach were carried out. The design stages and analysis results of the launch vehicle that will deliver the cubesat to the stratosphere layer are shared. In this study, a design exercise for a stratospheric rocket is proposed. Future research will examine the launch vehicle that will cross the space boundary, known as the Kármán line.

Keywords

Launch vehicle
Rocket
Cubestrat
Design
Analysis
Stratosphere

Time Scale of Article

Received 23 August 2022
Revised until 19 May 2023
Accepted 19 May 2023
Online date 28 June 2023

1. Introduction

Since ancient times, people have looked for means to travel to space. With new launch vehicles, it is now simpler to approach the space frontier, or the Kármán line. Cubesats are trained in the stratospheric layer. Every year, more man-made satellites are launched into orbit.

Since cubesat technology has advanced, they have begun to take the role of large satellites. The launch systems' main function is to raise the payload to the required, healthy altitudes. There are low-altitude, medium-altitude, and high-altitude launch methods available based on altitude. In practice, the most used methods to raise the payload to the desired altitude are rocket and atmospheric balloon technologies, which are much more cost-effective (Hall et al., 2020). Rocket propulsion is a class of jet propulsion in which stored mass, known as propellant, is combusted and ejected from the vehicle at high velocity (Balmogim et al., 2015). The launch vehicle is rocket type. Three components make up most launch systems. They are the propulsion subsystem, the structural subsystem, and the payload. A large part of

*: Corresponding Author Alper Şanlı, alpersanli16@gmail.com
DOI: 10.23890/IJAST.vm04is01.0102

launch systems is the propulsion system. There are main classes of propulsion systems; liquid rocket engines, solid rocket engines, hybrid rocket engines, nuclear rocket engines, electric rocket engines (Sutton and Biblarz, 2016). Liquid propellant rocket engines contain complex systems (McCormick et al., 2005). Hybrid rocket technology uses both liquid and solid fuel rockets (Dyer et al., 2007). The use of hybrid rockets is more efficient for launch vehicles (Leverone, 2013). Cesaroni reloadable rocket engines are considered in this study. This technology is convenient and less complex systems (Mahjub et al., 2020). The structural subsystem holds the other subsystems together, ensuring the launch vehicle's in flight integrity. The payload may be experimental, depending on the launch vehicle's mission. Launch vehicles can be employed for scientific, military, and academic endeavors.

Lift and drag on the launch vehicle can only be applied if the launch vehicle is in an atmosphere. The atmosphere consists of troposphere, stratosphere, mesosphere, thermosphere and exosphere layers. The mission of the launch vehicle designed and analyzed in this study is to deliver the cubesat to the stratosphere layer. The stratosphere layer is located between 12 and 50 km. Launching the launch vehicle in different seasons causes approximately 5% change in vehicle performance. The pressure in the stratosphere layer is between 200 mbar and 0 mbar. Atmospheric density is between about 0.3 kg/m^3 and 0 kg/m^3. Temperature values are between -60 °C and 0 °C. The wind speed at this altitude is 10 m/s and 60 m/s.

The launch vehicle that will take the cubesats to the stratospheric layer has been designed and analyzed for this project. Vehicle studies will be conducted in the following stages to transport the cubesats to the Kármán line. A launch vehicle that would send cubesats to the stratospheric layer for educational reasons was investigated before the Kármán line.

2. Overview of Mission

A launch system is created in this study to lift a cubesat intended for educational purposes into the stratospheric layer. Scientific data, image and telemetry data obtained from the atmosphere will be transmitted to the ground station through the sensors on the cube satellite used for educational purposes. There are two stages in the launch system. Three rocket engines are in the first stage, one rocket engine is in the second stage. The cubesat will be positioned in a location on the second level. POD with space for three 3U cubesats. At apogee altitude, POD will assist in releasing the cubesat from the launch vehicle. The sample cubesat model that can be launched with the launch vehicle and the model that can be mounted inside the launch vehicle of the sample cubesat model are shown in Figure 1.

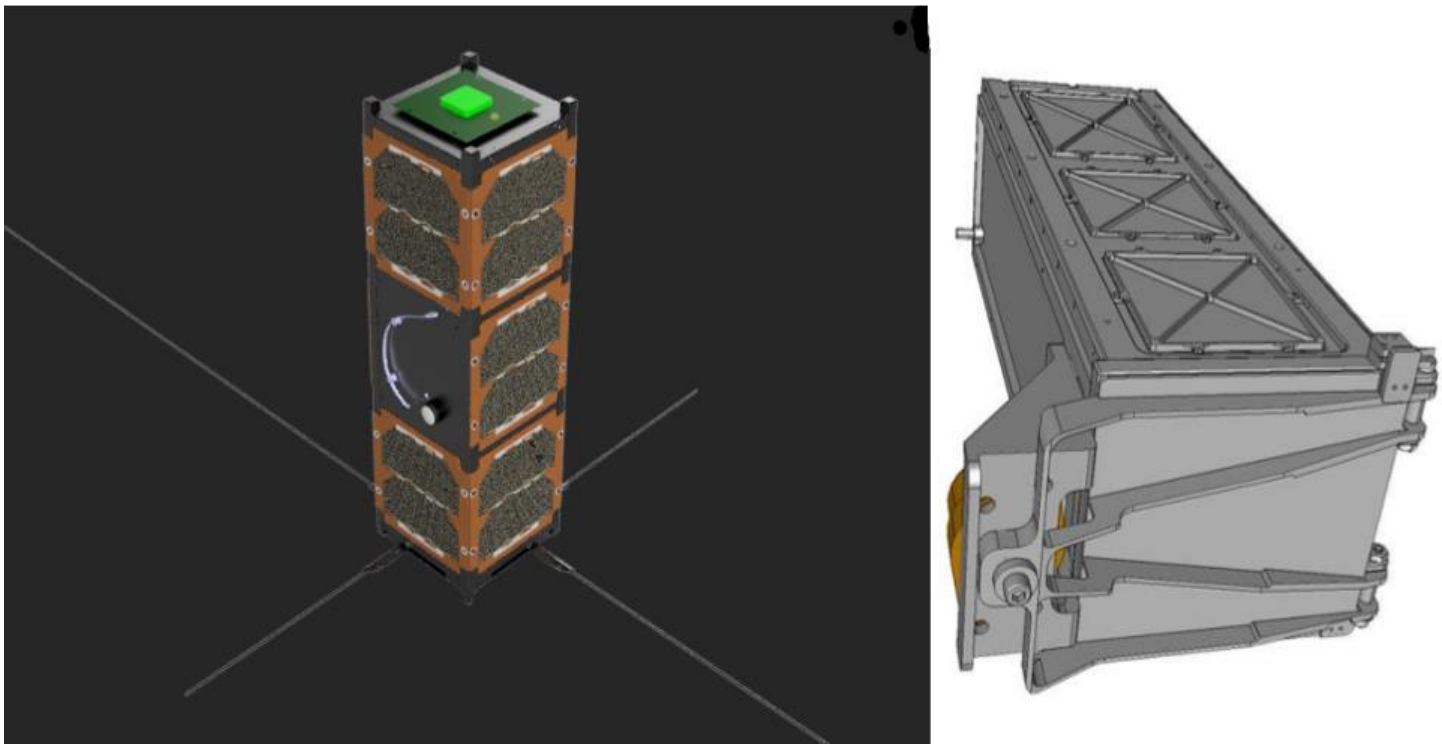

(a) (b)

Fig. 1. (a) Sample cubesat model and exploded view to be placed within the launch vehicle and simulation and (b) example of a cubesat that can be mounted on a launch vehicle (Şanlı and Aslan, 2021) (Johnstone, 2020).

3. Launch Vehicle Architecture and Details

Cubesat launch vehicles are still being developed today. Their goal is to place cubesat on the Kármán line. The launch vehicle must have the boundary conditions to carry the cube satellite. Cubesat dimensions are in 3U standards for this launch vehicle. The created design should be suitable for atmospheric conditions and should not damage the cubesat.

It is possible to classify rockets according to the Mach number. This number is the ratio of the velocity of a moving mass to the speed of sound under the conditions in which the mass is present. There are 6 regimens according to the Mach number. These are subsonic, transonic, supersonic, hypersonic, high-hypersonic and re-entry speeds. The values of Mach regimes are shown in the Table 1.

Table 1. Flight speed values according to regime types

Regime	**Flight Speed**				
	(Mach)	(knots)	(mph)	(km/h)	(m/s)
Subsonic	<0.8	<530	<609	<980	<273
Transonic	0.8-1.2	530-794	609-914	980-1,235	273-409
Supersonic	1.2-5.0	794-3,806	915-3,806	1,235-6,126	410-1,702
Hypersonic	5.0-10.0	3,308-6,615	3,806-7,680	6,126-12,251	1,702-3,403
High-Hypersonic	10.0-25.0	6,615-16,537	7,680-19,031	12,251-30,626	3,403-8508
Re-entry speeds	>25.0	>16,537	19,031	>30,626	8,508

It is a launch vehicle design that reaches supersonic velocity. Vehicles reaching supersonic velocities are in the 1.2–5.0 mach range. Equation 1 contains the formula for Mach number.

$$M=u/c \quad (1)$$

M :Mach number

u :The local flow velocity relative to the limits (m/s)

c :Constant for speed of sound in the medium (m/s)

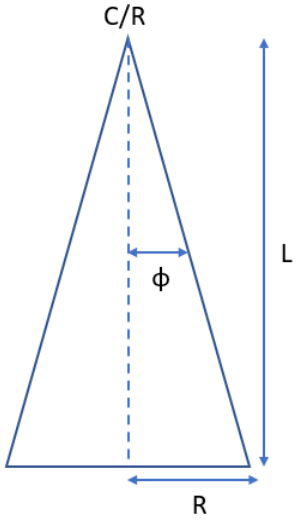

Fig. 2. Nose cone geometry

The maximum velocity of the designed launch vehicle is Mach 3.61. The designed launch vehicle is 419 cm long and weighs roughly 106602 g in total, including the payload. Fiberglass, carbon fiber, aluminum and a composite materials are frequently used materials in the launch vehicle. The strength of the materials is high and it provides structural strength. They are resistant to high temperatures and are lightweight materials. Fiberglass makes up the nose cone, while carbon fiber is used to build the stages and fins.

The boundary conditions of the cubesat must be compatible with the POD dimensions. The cubesat will be placed in a POD portion that is 30 cm long and 17 cm in diameter. On the launch vehicle, the POD section is in the second stage. When the launch vehicle reaches the desired altitude, it will release the cubesat from the POD section with a spring-loaded release mechanism. In this way, the cubesat and the launch vehicle will be separated

Launch systems can use conical, biconical, power series, ogive series, elliptical, parabolic, and haack series nose cones. The coefficient of friction is directly influenced by the nose cone design. The nose cone of the cubesat launch vehicle is conical in shape. Figure 2 shows the geometric design of the conical shape.

The drag coefficient change depending on the nose cone geometry is shown in Figure 3. These are rectangular, wedge, airfoil, rounded geometries. As the nose cone angle increases, the drag coefficient increases.

The variables in Equations 2 and 3 were used to design the nose cone geometry.

$$y = x\frac{R}{L} \quad (2)$$

$$\varphi = tan^{-1}(\frac{R}{L}) \quad (3)$$

x :position in reference plane

y :Position in reference plane

R :The radius of the nose cone

L :The length of the nose cone

φ :nose cone angle)

The nose cone in question weighs 585 g. The length of the nose cone is 600 mm, and the semi-structure is 170 mm. The design values of the nose cone are important for stable flight. Since it is the part that first encounters the fluid air, the drag coefficient should be low.

The dimension and visualization of the launch vehicle are shown in Figure 4. Drag is further reduced by limiting fuselage diameter (using the transonic area rule) at the fin-can section. The vehicle also features a conical tail piece to reduce base drag effects during subsonic flight (Brooks et al., 2010). There are four types of drag acting on the launch vehicle. These are friction drag, pressure drag, induced drag and interference drag (Box et al., 2009). Pressure drag is divided into two. These are wave drag and base drag. Friction drag occurs between the produced material and the fluid. Pressure drag is the difference in force caused by the pressure distribution around the launch vehicle. Wave drag is caused by the force differences that occur during shock waves. Due to the design of the launch vehicle, the velocity of the flow varies, which creates base drag. Induced drag occurs depending on the angle of the launch vehicle. Interference drag is caused by the interaction of the launch vehicle's fuselage and fins. Drag values are important for the launch vehicle to reach the desired altitude steadily.

The launch vehicle has fins that ensure stable flight. There are a total of six ailerons on the first stage and second stage. The blade sections are usually four. These are rounded, airfoil, wedge, rectangular geometries. The rounded blade geometry is easy to manufacture and provides average performance. Airfoil fin geometry is good for subsonic flight. The wedge blade geometry is good for supersonic flight. The rectangular blade geometry is easy to manufacture and has a high drag value. The launch vehicle has a wedge type fin geometry. The types of fins used in the launch vehicle are shown in the Figure 5.

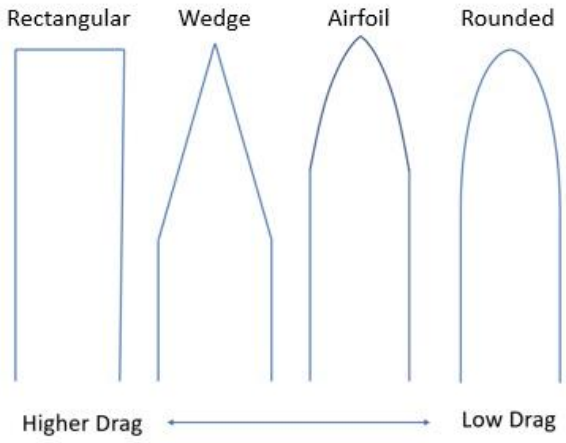

Fig. 3. Drag values according to geometric designs

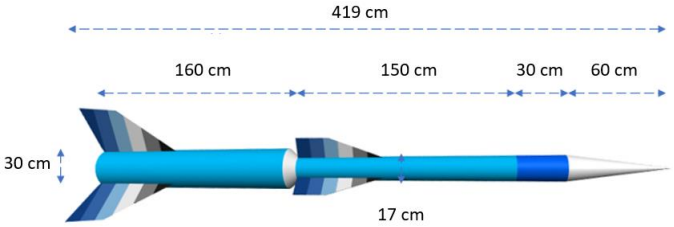

Fig. 4. Image and dimensions of the launch vehicle

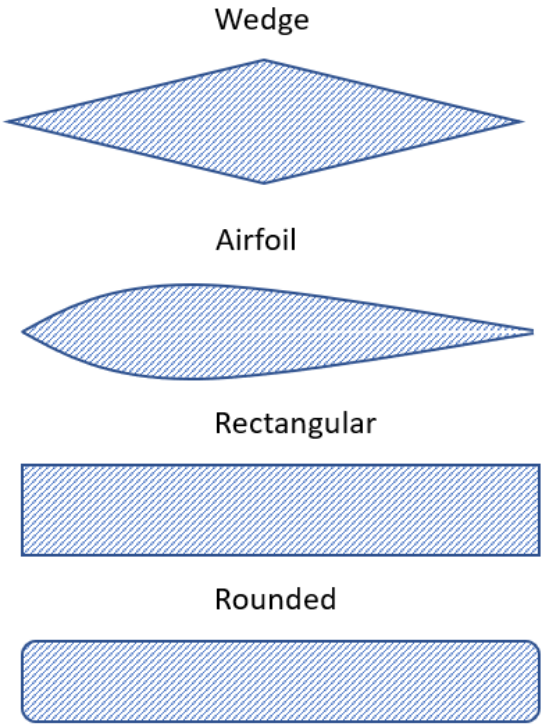

Fig. 5. Launch vehicle fin types.

The conical nose cone's overall drag coefficient was calculated to be 0.02. The center of pressure of the launch vehicle is directly impacted by the fin type chosen. Fins stabilize the launch vehicle because it lacks active control mechanisms. Control mechanisms provide a stabilized flight (Bossert et al., 2003). The

launch vehicle's center of gravity is positioned behind the center of pressure to ensure a steady flight. In total, 6 blades—3 in the first stage and 3 in the second—were employed. Ailerons used in the second stage have a total drag coefficient of 0.02 and blades used in the first stage have a drag value of 0.05. Equation 4 contains the formula for the drag force (Taylor, 2017).

$$F_D = C_d \rho V^2 \frac{A}{2} \quad (4)$$

F_D :Drag force (N)

C_d :Drag coefficient

ρ :Atmospheric density (kg/m^3)

V :Velocity (m/s)

A :Surface area (m^2)

The launch vehicle's architecture is depicted in Figure 6 and consists of two stages connected in series.

The launch vehicle is equipped with reloadable rocket engines. A rocket engine with a cylinder diameter of 161 mm and a length of 597 mm and a total impulse value of 41125 seconds is located in the second stage. Three Cesaroni rocket engines with a combined impulse value of 21041 seconds, a radius of 98 mm, and a length of 1239 mm are located in the first stage. I_s, the equation for the total impulse, is part of Equation 5 (Mishra et al., 2021).

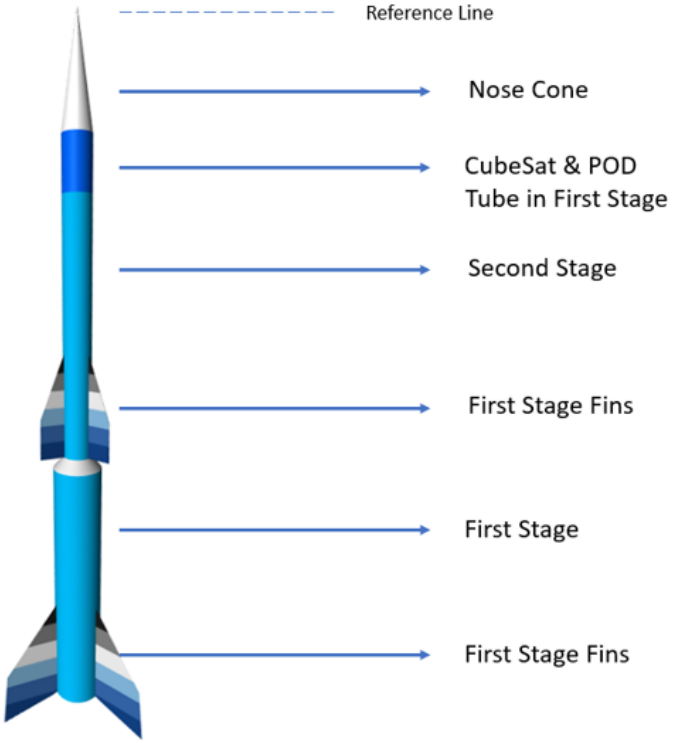

Fig. 6. Design and subsystems for launch vehicle

$$I_s = \frac{\int_0^t F dt}{g_0 \int_0^t \dot{m} dt} \quad (5)$$

$$c = I_s g_0 = \frac{F}{\dot{m}} \quad (6)$$

I_s :The total impulse (s)

F :Force (N)

t :Time (s)

$\dot{m}$:Total fuel mass burn rate (kg/s)

g_0 :Gravity acceleration (m/s^2)

With the help of engine blocks and gripping components, rocket engines are fastened to stage structures. The launch vehicle has a maximum speed of 3.61 Mach, a maximum acceleration of 170 m/s^2, and an apogee of 32676 meters. The launch vehicle's pressure center is 321 cm from the reference plane, whereas the center of gravity is 269 cm from the same reference point.

The center of gravity and center of pressure equations are found in Equation 7 and Equation 8. W (N) stands for the overall weight, c_g (mm) is the distance from the center of gravity to the reference plane, d_n (mm) is the distance of the subsystems from the reference plane, and w_n (N) is the weight of the subsystems. A_n (mm^2) is the surface area of the subsystems, and c_p (mm) is the separation between the center of gravity and the reference plane. The center of gravity and center of pressure on the launch vehicle are shown in Figure 7 and Figure 8.

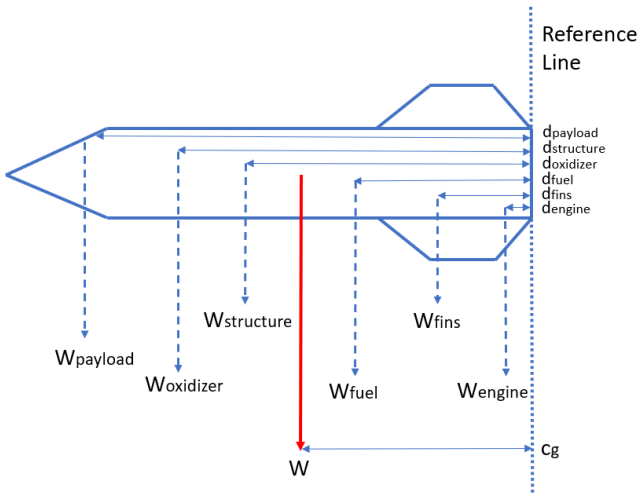

Fig. 7. Center of gravity on the launch vehicle

$$c_g = \frac{w_{payload} d_{payload} + w_{oxidizer} d_{oxidizer} + w_{fuel} d_{fuel} + w_{structure} d_{structure} + w_{engine} d_{engine} + w_{fins} d_{fins}}{W} \quad (7)$$

$$c_p = \frac{a_{payload} d_{payload} + a_{structure} d_{structure} + a_{fins} d_{fins}}{A} \quad (8)$$

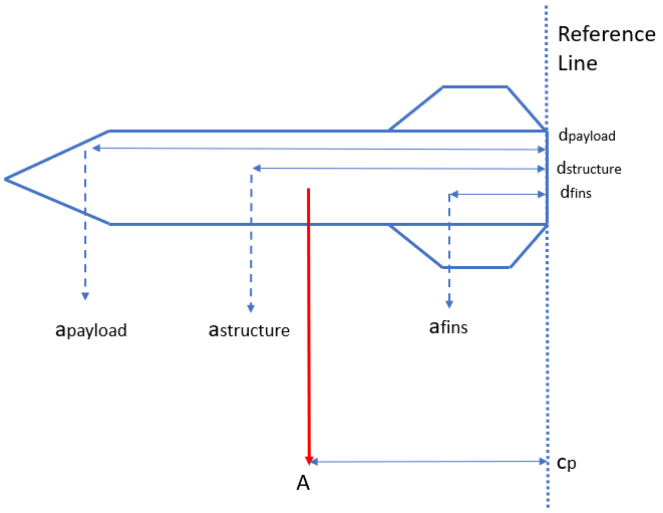

Fig. 8. Center of pressure on the launch vehicle

4. Results of Launch Vehicle Flight Analysis

The altitude, stability, center of pressure, center of gravity, and drag that the launch vehicle will reach during its flight are analyzed. The launch vehicle's stability is directly impacted by the position of the center of gravity and the center of pressure. It can ascend vertically due to its stability.

The launch vehicle consists of two stages. When the altitude of 2 km is reached, the first stage of the launch vehicle leaves. The first stage leaves the launch vehicle after 10-12 seconds. The second stage of the launch vehicle reaches an altitude of about 32 km and releases the cube satellite at the highest altitude. The launch vehicle reaches the highest altitude during 78-82 seconds of flight.

The total flight time of the launch vehicle took 725 seconds. The launch vehicle's total altitude values are shown in Figure 9.

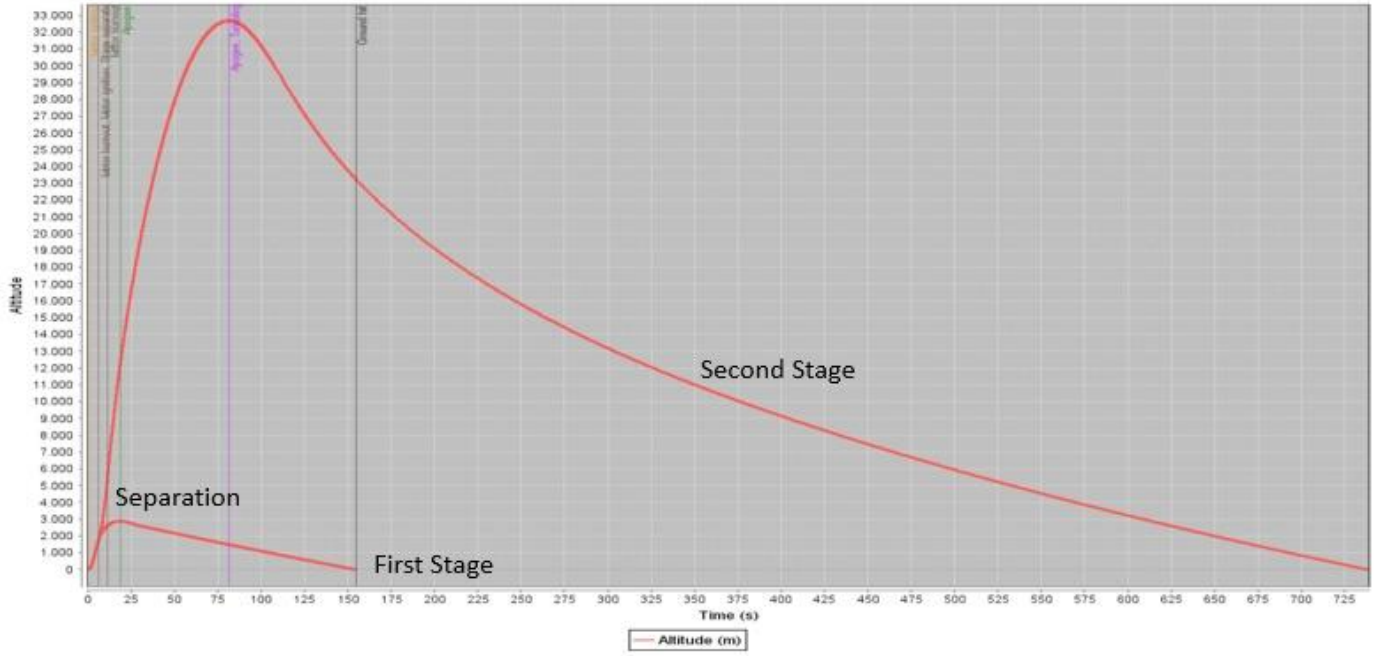

Fig. 9. Total altitude of the launch vehicle graph

The first stage of the launch vehicle split at about 3000 meters. This separation is shown by the red line in Figure 9. The second stage of the rocket reached an altitude of 32676 m. This is shown with a red line in Figure 10. The stable flight of the launch vehicle depends on the center of gravity and the center of pressure. During the flight, the center of gravity must be in front of the center of pressure in the reference plane so that the launch rocket can reach the highest altitude. The parachute will prevent the launch vehicle from being damaged by reducing its speed during its fall (Chowdhury, 2012). Parachute rescue will be made for the launch vehicle.

During the first 10 seconds of flight, the center of pressure is on average 100 cm behind the center of gravity. With the realization of the stage separation, the center of gravity is on average 25 cm ahead of the pressure center during the 80 seconds when the highest altitude is reached.

The shifts in the launch vehicle's center of gravity and center of pressure are depicted in Figure 10 over the course of its entire flight. The flight demonstrated a steady flying because the center of pressure did not cross in front of the center of gravity. It was discovered that the stability value was always positive.

In Figure 10, the Cp value changed from 320 mm to 150 mm at 8 seconds; Cg value decreased from 250 mm to

150 mm. This is because the first stage is separated from the launch vehicle. Throughout the duration of flight, the launch vehicle is subject to drag, which has an impact on its stability and altitude. The launch vehicle is exposed to friction drag, pressure drag, induced drag and interference drag during flight. The resulting shock wave is effective in the structure of the launch vehicle and in the formation of atmospheric drag. The pressure differences that occur in the launch vehicle structure during the flight cause different forces to act on each area of the launch vehicle.

According to the mach number value, the values of the drag coefficient, friction drag coefficient, base drag coefficient, and pressure drag coefficient are shown in Figure 11.

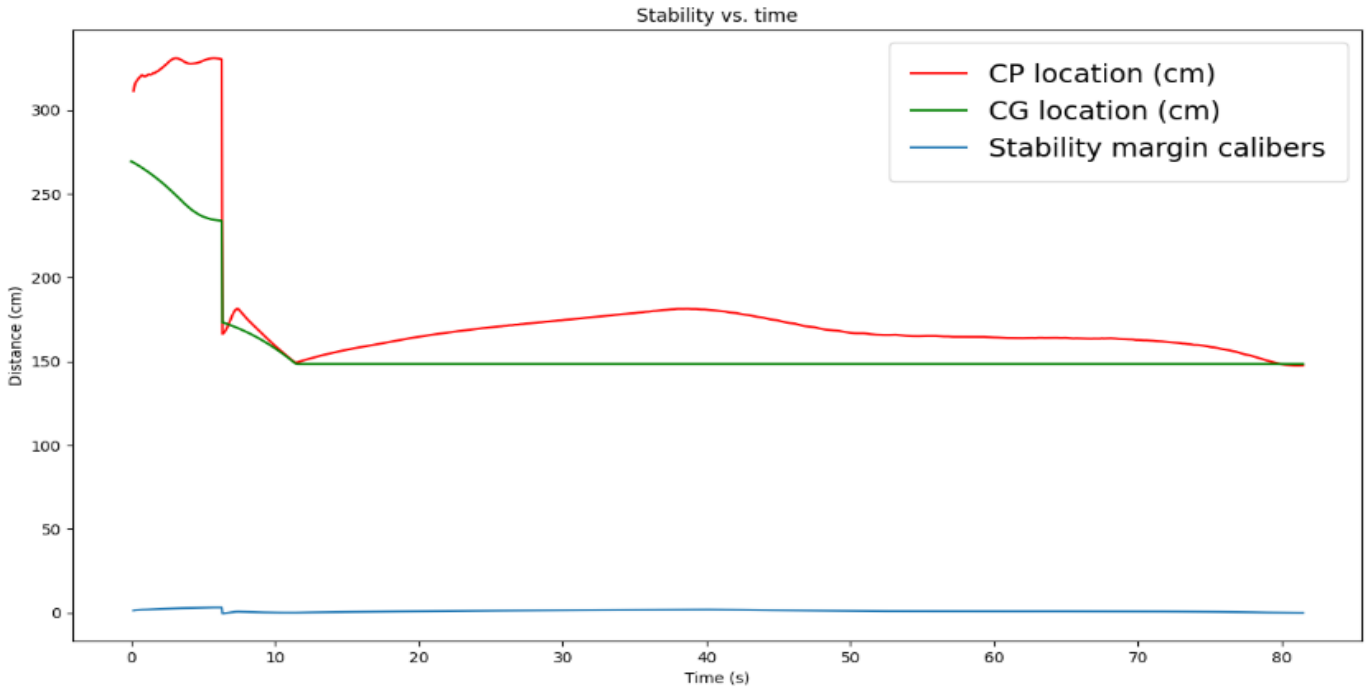

Fig. 10. Graph of launch vehicle stability over time

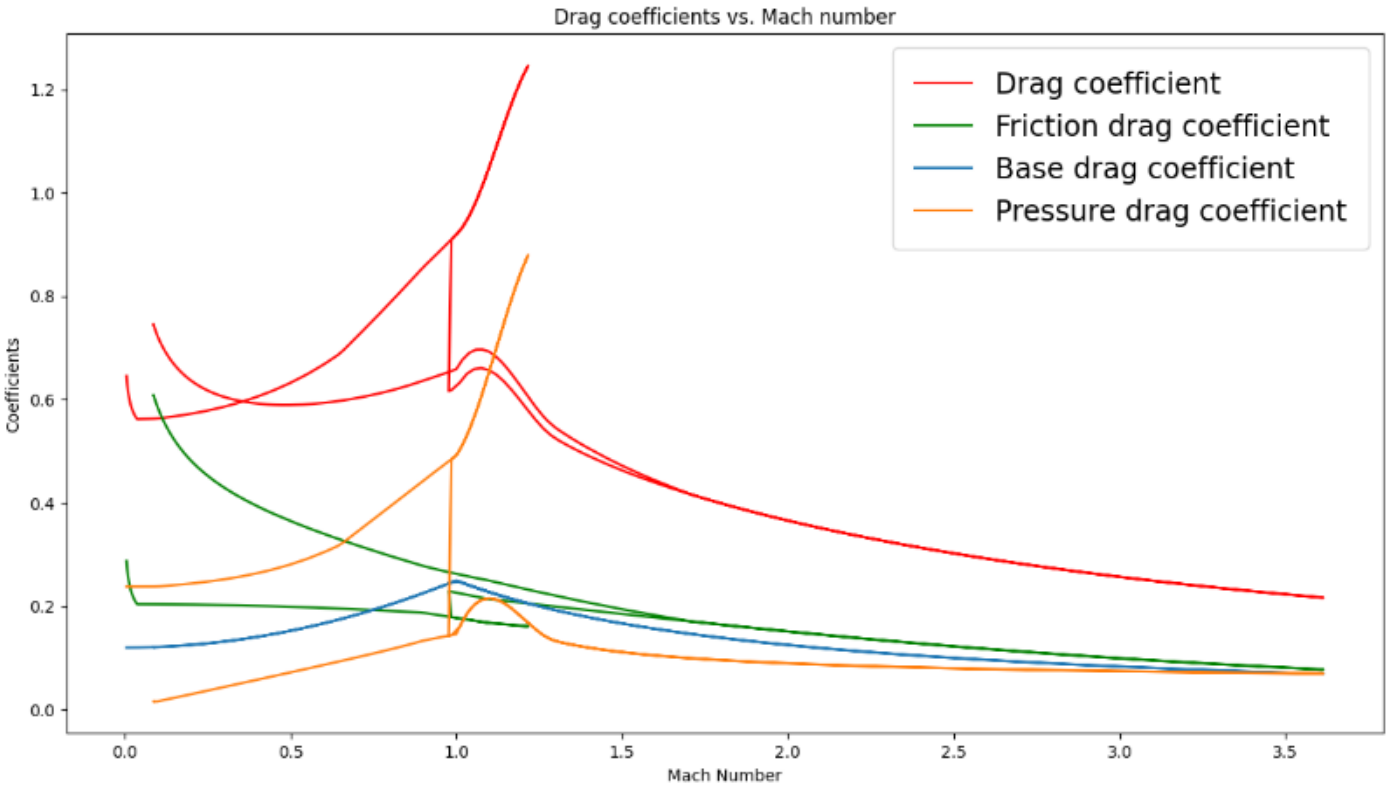

Fig. 11. Vehicle drag coefficients and a graph of the Mach number

Different forces due to pressure differences expose the launch vehicle to drags. Drag coefficient, base drag coefficient and pressure drag coefficient values show an increase up to 1 Mach level. The drag coefficient creates drag with a maximum value of 0.9. On the other hand, the friction drag coefficient value decreases. With the separation of the step, all drag coefficient values decreased. The largest drag type encountered at the 3.5 Mach level is the drag coefficient with a value of 0.25.

5. Conclusions

In this study, the launch vehicle that will carry the cubesat, which will be used for educational purposes, to the stratosphere layer has been full designed and flight analyzed. The design of the launch vehicle was carried out in accordance with the desired mission. The training cubesat was intended to be launched into the stratospheric layer in the earliest iterations of the launch vehicle. The cubesats will be dropped above the Kármán line in later iterations. Experiences were obtained by conducting a literature search.

In this study, the 10 kg payload was elevated to an altitude of 32676 m to create the launch vehicle design. The two stage launch vehicle has a total length of 419 cm and weighs 106602 g. The launch vehicle reaches supersonic speeds of Mach 3. Fiberglass, carbon fiber, aluminum and a composite materials were chosen to provide structural and thermal resistance at high speeds. A conical nose cone is designed to reduce the drag coefficient. Wedge type inactive ailerons are used to provide stable flight to the maximum altitude. Ailerons used in the second stage have a total drag coefficient of 0.02 and blades used in the first stage have a drag value of 0.05. Three reusable rocket engines were used in the first stage and one in the second stage. The launch vehicle has a maximum speed of 3.61 Mach, a maximum acceleration of 170 m/s^2, and an apogee of 32676 meters. The launch vehicle's pressure center is 321 cm from the reference plane, whereas the center of gravity is 269 cm from the same reference point.

Upon reaching an altitude of 3000 m, the initial stage of the launch vehicle separates, while the second stage ascends to approximately 32676 m, releasing the cubesat at its peak. The entire flight duration of the launch vehicle amounts to 725 seconds. Throughout the mission, stability is thoroughly examined and found to remain consistently positive. For the initial 10 seconds of flight, the center of gravity surpasses the center of pressure by an average of 100 cm. As the ascent continues for 80 seconds to the highest altitude, the center of gravity, on average, leads the center of pressure by 25 cm. The launch vehicle maintains a steady flight trajectory throughout its entire mission.

Different types of drag are discussed and analyzed. The drag coefficient, base drag coefficient, and pressure drag coefficient exhibit an increase up to the 1 Mach level. The drag coefficient reaches a maximum value of 0.9, generating the highest drag. Following the separation of the stage, all drag coefficient values decrease. At the 3.5 Mach level, the drag coefficient of 0.25 represents the largest encountered drag type.

In future studies, structural and flow analyzes will be examined in detail. A launch vehicle that can reach the Kármán Line, which is accepted as the space limit, and leave a cubesat, will be designed.

CRediT Author Statement

Alper Şanlı: Conceptualization, Methodology, Software, Investigation, Validation, Writing-Original Draft. **Tuncay Yunus Erkeç**: Conceptualization, Investigation, Resources. **Melih Beceren**: Conceptualization, Methodology, Software, Resources, Investigation, Validation, Writing-Original Draft. **Mehmet Furkan Kemallı**: Conceptualization, Methodology, Software, Investigation, Validation.

References

Balmogim, U., Brooks, M. J., Pitot de la Beaujardiere, J. F., Veale, K., Genevieve, B. and Roberts, L. W., 2015. Preliminary Design of the Phoenix-1B Hybrid Rocket. Orlando, 51st AIAA/SAE/ASEE Joint Propulsion Conference.

Barrowman, J.A., Theoretical Prediction of the Center of Pressure, Cambridge, 1966.

Bossert, D. E., Morris, S. L., Hallgren, W. F., & Yechout, T. R. (2003). Introduction to aircraft flight mechanics: Performance, static stability, dynamic stability, and classical feedback control. American Institute of Aeronautics and Astronautics.

Box, S., Bishop, C. Hunt, H., Estimating the dynamic and aerodynamic paramters of passively controlled high power rockets for flight simulaton, 2009.

Brooks, M. J., Pitot de la Beaujardiere, J. F., Chowdhury, S. M., Genevieve, B. and Roberts, L. W., 2010. Introduction to the Univeristy of KwaZulu-Natal Hybrid Sounding Rocket Program. Nashville, American Institude of Aeronautics and Astronautics.

Chowdhury, S. M., 2012. Design and Performance Simulation of a Hybrid Sounding Rocket,MScEng Thesis, Durban: University of KwaZulu-Natal.

Dyer, J., Doran, E., Dunn, Z., Lohner, K., Bayart, C., Sadhwani, A., Zilliac, G., Cantwel, B. and Karabeyoglu, A., 2007. Design and Development of a 100km Nitrous Oxide/Paraffin Hybrid Rocket Vehicle. Cincinnati, 43rd AIAA/ASME/SAE/ASEE

Joint Propulsion Conference and Exhibit.

Hall, H., Chamieh, M., Chu, J., Daruwala, R., Duong, V., Holt, S., ... & Stoica, A. (2020). Utilizing High Altitude Balloons as a Low-Cost CubeSat Test Platform. In 2020 IEEE Aerospace Conference (pp. 1-11). IEEE.

Johnstone, A. (2020). Cubesat Design Specification (1U-12U) Rev 14 CP-CDS-R14. The Cubesat Program, Cal Poly SLO, July.

Leverone, F. K., 2013. Performance Modelling and Simulation of a 100 km Hybrid Sounding Rocket, MScEng Thesis, Durban: University of KwaZulu-Natal.

Mahjub, A., Mazlan, N. M., Abdullah, M. Z., & Azam, Q. (2020). Design Optimization of Solid Rocket Propulsion: A Survey of Recent Advancements. Journal of Spacecraft and Rockets, 57(1), 3-11.

McCormick, A., Hultgren, E., Lichtman, M., Smith, J., Sneed, R. and Azimi, S., 2005. Design, Optimization, and Launch of a 3" Diameter N2O/Aluminized Paraffin Rocket. Tucson, 41st AIAA/ASME/SAE/ASEE Joint Propulsion Conference & Exhibit.

Mishra, A. K., Gandhi, K., Sharma, K., Sumanth, N., & Teja, Y. K. (2021). Conceptual design and analysis of two stage sounding rocket. International Journal of Universal Science and Engineering, 7(1), 52-72.

Sutton, G. P., & Biblarz, O. (2016). Rocket propulsion elements. John Wiley & Sons.

Şanlı, A., Aslan, A.R. (2021). Design of ASTINSAT-1 And Structural Analysis, Use of Generative Design. International Congress On Engineering And Technology Management.

Taylor, T. S. (2017). Introduction to rocket science and engineering. CRC Press.

International Journal of Aviation Science and Technology

Research Article

Maintenance 4.0: Automation of Aircraft Maintenance Operational Processes

Sally Ichou[1]*, Arpad Veress[2]

[1] Department of Aeronautics and Naval Architecture, Faculty of Transportation Engineering and Vehicle Engineering, Budapest University of Technology and Economics, Műegyetem rkp. 3., H-1111 Budapest, Hungary
sallyichou93@gmail.com - 0000-0002-4014-7977

[2] Department of Aeronautics and Naval Architecture, Faculty of Transportation Engineering and Vehicle Engineering, Budapest University of Technology and Economics, Műegyetem rkp. 3., H-1111 Budapest, Hungary
veress.arpad@kjk.bme.hu- 0000-0002-1983-2494

Abstract

The advancement of technology is ramping up the pace of digitization and automation of aircraft maintenance activities, and with that, the stakeholders' interest in high-level technology has also increased over the past few years. Thus, to stay relevant in the market and capable of competing, Aircraft Maintenance and Overhaul (MRO) companies must reshape and adapt to newer methodologies to enhance and enrich the quality of aviation and after-sales services. Operational processes are essential to any successful business because it plays a vital role in the efficient and effective functioning of the organization and structure of the enterprise. Hence, this paper will focus on the possibilities of automation and data integration into the daily operational workflow, its contribution, and its influence on the industry. And since the initiation of Industry 4.0, newer opportunities and possibilities have arisen to investigate decision-making algorithms, their influence on overall job quality and precision as well as the synergy between humans and machines and their cooperation in the operational areas of the maintenance process.

Keywords

Aircraft maintenance
Industry 4.0
Automation
Operational process development
Artificial intelligence

Time Scale of Article

Received 30 December 2022
Revised until 5 April 2023
Accepted 13 May 2023
Online date 28 June 2023

1. Introduction

Technology has effectively changed how companies connect and interact with their consumers, allowed stakeholders to make more strategic choices, and create smoother workflows. Data analysis enables enterprises to take informed moves toward operational efficiency with more confidence. With the introduction of the 4th industrial revolution, it is now possible to integrate complete digitalization and a high level of automation into the operational and professional structure of every company. Hence, reducing the necessity for direct human intervention.

The increasing amount of data generated in Industry 3.0, together with enhanced computational abilities and the usage of Business Analytics (BA), paved the path for Artificial Intelligence (AI) to be employed during this period, allowing a substantial amount of information to be processed by machines and computers. The Internet of Things, Big Data analysis, and machine learning are the cornerstone technologies of Industry 4.0, this term applies to the implementation of advanced information technologies in industries and is often used for the digital revolution. In Industry 4.0, AI integrates numerous technologies that enable software and machines to sense, comprehend, act, and learn human operations.

Maintenance has carved out a large portion of the industry's research budget for the following development release. It can benefit from BA and data

*: Corresponding Author Sally Ichou, sallyichou93@gmail.com
DOI: 10.23890/IJAST.vm04is01.0103

collection to lower the likelihood of a system or component failure and related costs.

AI was considered a potentially beneficial tool by many institutions, research centers, and even industries to address the obstacles and challenges that MRO firms confront. The large number of papers and publications on this subject reflect the high degree of interest in these applications in maintenance management, scheduling, and planning, as well as the notion of developing an intelligent maintenance optimization system.

Furthermore, it is clear that aviation technology is advancing toward more sustainable and environmentally friendly solutions, which means that maintenance operations must be able to satisfy those new standards accurately while being cost-effective.

MRO aims to preserve the aircraft's airworthiness and reliability to high levels, and as the number of flights has risen so did the need for aircraft availability. As a result, organizations in this industry must invest in their skills and experiences to assure high-quality work and market competitiveness. So, according to this fast and continuous development and growth in the aviation sector, the MRO model has matured to noticeable levels in the past few years, it evolved from being reactive and human-based to being more automated and sustainable, as it is illustrated in Fig. 1.

It is difficult to predict when complete automation and entirely computerized decision-support agents in MRO will be reached as it is dependent on several variables such as technical developments, legal frameworks, and industrial acceptance. However, it is more likely to see further development in this path over the next several decades. For example, the Federal Aviation Administration (FAA) set a target almost a decade ago to achieve the lowest possible aircraft accident rate caused by 2025 (FAA, 2011), this safety plan is still a goal today and will continually necessitate higher levels of automation and AI incorporation in MRO operations.

Currently, the technology in this field has reached level 3 of maintenance maturity, and with the assistance of huge data sets, trend recognition with high accuracy and efficiency will be realized and pave the way for full automation in decision-making without human intervention. Therefore, the results will be an increase in efficiency, preparedness for future events, and a decrease in delays and costs.

There are already ongoing effort attempts to create more sophisticated AI systems for MRO, such as the use of machine learning algorithms for predictive maintenance and problem diagnostics. However, regulatory obstacles, as well as worries about safety, reliability, and cybersecurity, may restrict the implementation of completely autonomous systems.

Predicting the duration of maintenance tasks is one area where AI could show great potential. Accurate scheduling and planning are critical in MRO operations because it helps to optimize aircraft Turn Around Time (TAT) and reduce delays and outages. However, determining the time length of maintenance tasks can be complex and difficult because it depends on many variables such as the task's complexity, the availability of tools and equipment the technician's experience and skill, and the unknown damages/problems. Hence, the purpose of this article is to investigate the use of AI for estimating the performance time of maintenance tasks, as well as to examine the current state of the art and find possibilities for further research and development.

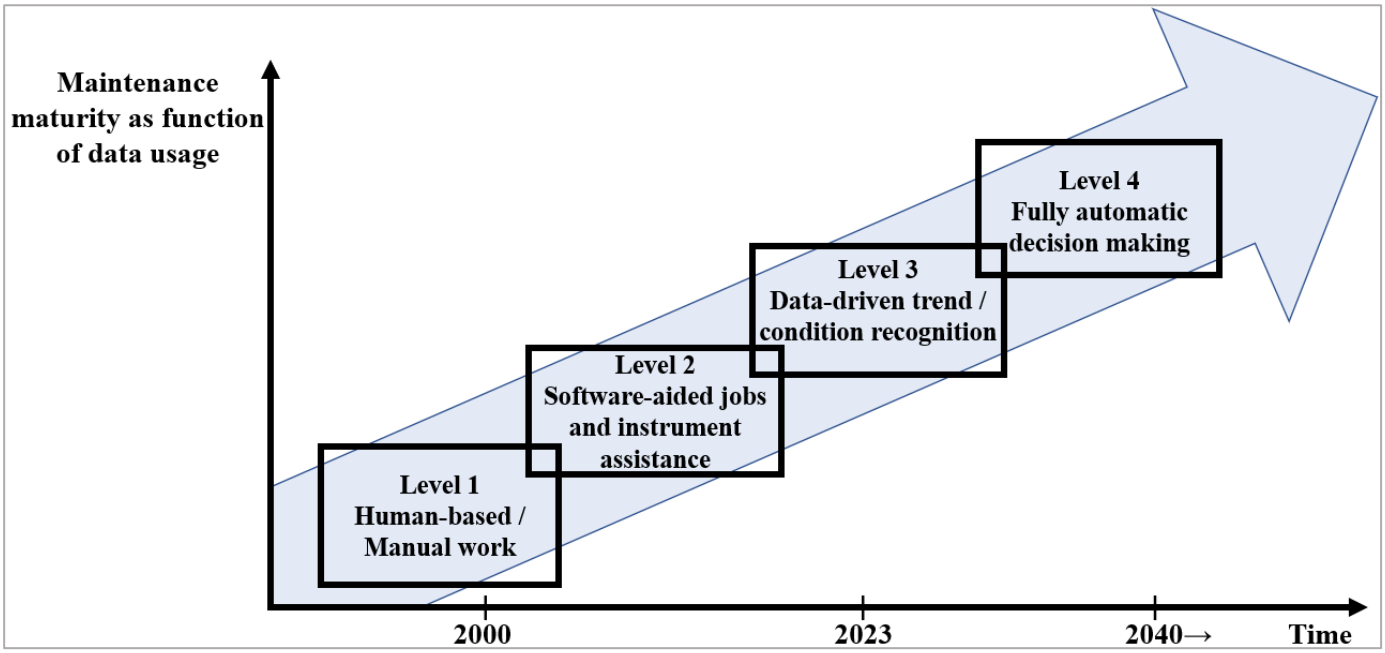

Fig. 1. The maturity of operational maintenance over time as a function of data utilization

This research will begin with a summary of the daily routine and current challenges facing MRO procedures, it will then go over the state of the art of AI integration in MRO processes, going over the different methods and algorithms that have been used to forecast and improve accuracy in MRO operations. Then a neural network module will be suggested to evaluate its ability to detect repeated patterns in task time prediction. Finally, the conclusion will highlight future research and development areas, examining how AI can be further incorporated into MRO operational workflow to enhance aircraft efficiency, safety, and dependability.

2. Method of automation and AI integration in MRO Operational Processes

2.1 Key Elements of MRO Operations

The goal of aircraft maintenance, repair, and overhaul services is to guarantee high reliability, safety, and airworthiness levels. Several maintenance actions are carried out to achieve these goals following the customer's customized Aircraft Maintenance Program (AMP) which is initially developed from the Maintenance Planning Document (MPD) in addition to any extra tasks needed by the aircraft manufacturers or aviation authorities. This can include Service Bulletins (SBs), Airworthiness Directives (ADs), or other requirements specific to the aircraft's configuration, model, or operation environment such as customer-specific additional jobs (FAA, 2016).

The scope of work performed when completing the related types of maintenance is set by the manufacturer's maintenance requirements, which are coordinated with national civil aviation authorities with a common target of restoring and maintaining the aircraft's ability to work, delaying aging of structure elements, preventing/correcting possible malfunctions, and upgrading software and computers ensuring that the highest amount of safety possible.

When a set of work orders or tasks are given to the MRO company to be performed on a specific aircraft, the MRO will give the operator/customer of the aircraft an estimated time for finishing the check and in accordance with that, the contracts will be signed. This time is called Turn Around Time (TAT) and it is extremely crucial for the entire maintenance process since the airlines strive to keep their planes in the sky, in other words, aircraft on the ground are not making a profit but on the contrary, they are costing money.

Therefore, keeping the agreement and delivering the aircraft back on time is one of the key elements of competitiveness in the market, the process of delivering the aircraft on time comprises of the proper coordination of all resources involved to ensure aircraft punctuality and keep operators waiting as little as needed. But a the same time performing excellent maintenance work in order to ensure that the aircraft is reliable and airworthy.

However, in an environment that is characterized by having a lot of uncertainties and emergency occurrences, it is quite challenging to accurately forecast the future manually without the help of data-generated modules and algorithms which is why it is easy to find a lot of research in the pipeline for such innovations.

2.2 The State of the Art in AI Integration for MRO Operations

Building correct modules and enhancing them by AI is not newly investigated for MRO, and when a work environment is known for having a lot of uncertainties, the focus was always focused on finding better ways to make correct predictions and developments in various fields of maintenance to make the work a bit more organized. With the help of Big Data, the Internet of Things (IoT), and AI techniques such developments surfaced and gain popularity. For example, Knowledge-Based Systems (KBS) were used in diagnostics decisions (Acosta et al., 2006), troubleshooting (Bello, 2016), HR management, and scheduling. The architecture of KBS systems is illustrated in Fig. 2.

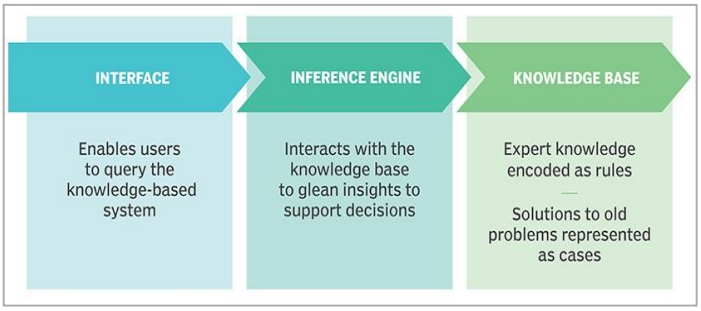

Fig. 2. The architecture of KBS system (Moore, 2019)

Case-Based Reasoning (CBR) is another famous sort of experience-based methodology that can effectively obtain knowledge from previous situations and solve new problems. Since this kind applies several human intelligence traits such as learning and memory, it is widely used for planning, problem-solving, and reliability analysis (Kolodner, 1992). Furthermore, until today this type of AI is still being explored lately it was used to not only give a diagnosis but also to give maintenance decisions according to historical data (Xie *et al.*, 2020). The CBR systems work process is illustrated in Fig. 3.

Fuzzy logic (FL) is also quite popular in MRO operational applications, is a developed form of Boolean logic, where the logic is either truth or fault (1 or 0) that today's computers are based on. The method uses "degrees of truth" in addition to extreme "yes or no" cases as illustrated in Fig. 4, it mimics how a person would make

decisions, only much faster therefore this system is effective for engineering cases without precise data or for uncertain cases, such as natural language processing (Zhou et al., 2021), machine input, and output controls, maintenance modeling, and risk-based inspection programs (Djenadic et al., 2022).

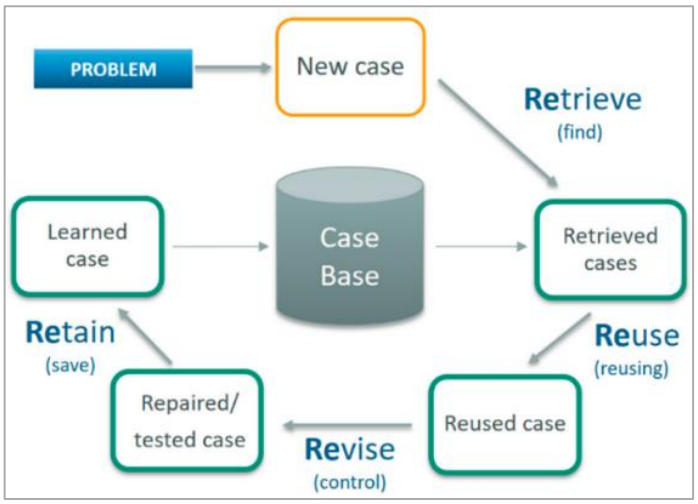

Fig. 3. CBR systems work process (Pusztová, et al., 2021)

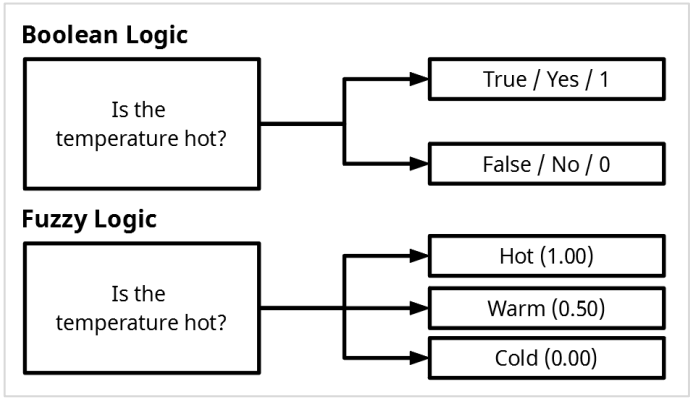

Fig. 4. Difference between Fuzzy and Boolean logic (Sioson, 2020)

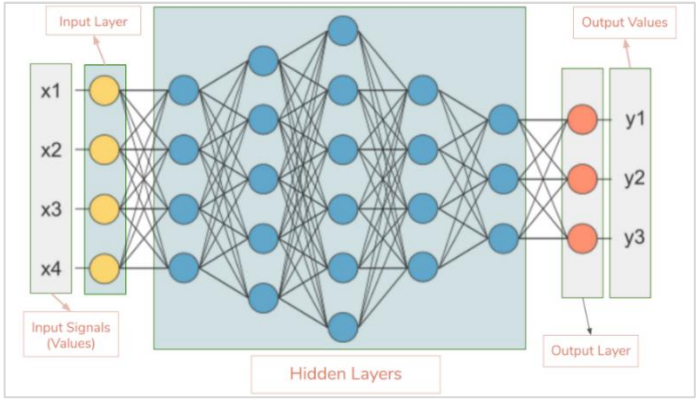

Fig. 5. Example of a simple ANN layout (Mate Labs, 2017)

The ANN system is made up of several parallel-connected processors that are organized into levels or classes. The first level of processors gets the raw inputted data, the second level receives the output data of the level before it (no longer raw data), and so on until the output data of the last level of processors is reached, which is the system's output (see Fig. 5). ANN are incredibly adaptive systems that learn from prior experience and training.

Of course, there are hybrid systems also, which are the combination of two or more AI types together to achieve optimum performance.

2.3 Improving Turn Around Time (TAT) Accuracy in Aircraft Maintenance with Artificial Intelligence (AI)

In the areas of predicting the correct time duration for performing maintenance tasks, AI deployment in the field of MRO processes is still not fully explored as much as it is in other industries. For example, in manufacturing and production processes, deep learning is frequently employed in predicting the time it will take to complete a certain product (Huang, Chang, and Arinez, 2020). But, in those investigations, the trend in human performance is not studied.

In aviation, the Original Equipment Manufacturers (OEMs) try to estimate the number of man-hours required to perform various maintenance tasks, usually, it is based on average values determining the time needed for a regular mechanic to perform the job with the correct tools, support, and equipment (Sasadmin, 2014). This estimation can be a bit over-optimistic for operators and MRO facilities because technicians' and mechanics' competency varies from one MRO to another, so every company will introduce a factor based on its team efficiency and it can be anywhere from 1.25 times to 4 times the recommended OEM recommendation.

The problem with that factor is that it is fixed, it doesn't take into consideration the aircraft's age, the experience of the technician, or the limitations and constraints that are facing the activities. The real performance time or the actual human man-hour of performing tasks can alter and change the original TAT and thus delay the release of the aircraft. So accurately predicting this value can be a game changer in MRO workflow.

MRO planners frequently anticipate the number of manhours needed for either scheduled or unplanned MRO duties resulting from historical inspection reports. Accurate forecasting can boost the productivity and revenue of MRO operations while also reducing turnaround time for aircraft operators. Hence, forecasting techniques and distribution functions were used to improve job time prediction with the help of data analytics (Pelt, Stamoulis, and Apostolidis, 2019) (Pelt and Stamoulis, 2018).

Another example from the scientific world is a time

duration estimation for ship refit (deck painting task) that was forecasted using hybrid - historical data/human experts inputs – and the sklearn decision tree classification algorithms to train the prediction models. The results showed improvements in the estimation accuracy by 5 – 10% (Li and Lafond, 2023).

As indicated from the literature research accurate task duration prediction is an extremely important aspect of aircraft project management. Hence, keeping the agreement between the maintenance provider and the customer and for the scheduling and optimizing of maintenance planning.

2.4 Methodology and Data Generation

The precision of ANN will be tested in this paper by the usage of dummy data by utilizing a similar approach to the ones used in previous research with a special focus on the multi-layer perceptron regressor which belongs to the ANN.

The Multi-layer Perceptron (MLP) is a supervised learning method that learns the function:

$$f(.) : R^m \rightarrow R^o \quad (1)$$

By training on a dataset, where "m" is the number of dimensions for input, and "o" is the number of dimensions for output, given of set of features (inputs X= $x_1, x_2 \ldots\ldots, x_n$) and a target (output y) it can learn a non-linear function approximator for regression problems (Scikit-learn, 2019).

To test the capability of the ANN "random dummy (synthetic) data" was generated according to Table 1.

All the values are manually generated values, structured in a way that will allow to test if the ANN is actually capable of noticing a trend in the performance time and accordingly predicting future events. For example, by looking at the employee's age, it is generated by giving one random employee a random age. Similarly, the task number is given a random number and each task number will have a random planned time.

When creating the data and to know the accuracy and precision of the module, a random function was defined to generate the value of the "actual man-hour" in Excel. These values were fed to the ANN module as a two-dimensional data frame in a CSV file form containing numbers. If the module understood the trend and was able to predict it correctly, it means that it could be used on real-life data.

The ANN module will be trained by the following data set (see Table 2), it consists of 6000 rows and 8 columns. The more columns we have in the dataset the more rows we need to train the neural module. The inputs should be defined based on the input data we want to analyze, so the ANN model that will be used will have 7 inputs. The actual time column is not counted in because it is the output of the prediction. Therefore, the output will consist of only one neuron which is the actual time. In other words, the module will base its actual man-hour prediction on task number, planned man-hour, the employee who performed the task, the employee experience, the employee's age, the aircraft age, and the aircraft Manufacturer's Serial Number (MSN).

The 6000 rows of data were divided into two parts, the first 99% of the set will be used for training, and the remaining 1% will be used as a test set for the trained module. Before training, pre-processing was done by means of standard scale which is a function in "scikit-learn" more known as "sklearn" inside a machine learning python package, because it improved the accuracy.

Table 1. Dummy data descriptions for the aircraft maintenance task

ID	Feature	Description	Type	Value Range
1	Task Number	Input	Integer	index [1007378, 9998413]
2	Planned Time	Input	Float	[0.01, 10]
3	Performed By	Input	Integer	[1, 50]
4	Actual Man-hour	Output	Float	[1.29, 101.5]
5	Employee Age	Input	Integer	[22, 50]

Table 2. The dummy data was used to train the ANN module

Task	Planned Man-Hour	Performed By	Actual Man-hour	Emp. Age	Emp. Experience	MSN	A/C Age
8139944	1.23	employee_3	1.68	45	22	200	23
8642378	0.06	employee_7	1.68	39	4	600	19
4105888	2.67	employee_9	3.41	29	8	600	19
…	…	…	…	…	…	…	…
2140896	0.19	employee_2	1.61	35	10	300	22

3. Results and Discussion

After training, and by using the test data set the results are as illustrated in Fig. 6, it is noticed that the neural network was able to predict accurately the actual man-hour needed for the task specified, and it noticed the trend for each employee/technician working on the tasks.

The aircraft age also played a role in defining the time needed for finishing the task. The module, based on the data given for training, presumed that the older the aircraft the more it would take to finish the job, which is not always the case in real life because not all tasks will have that effect. For example, servicing tasks such as lubrications and changing filters won't be affected by the age of the aircraft in general. So, this will need to be tested with different datasets to see if the module can recognize it.

Fig. 6 clearly shows the results of the predictions, by comparing the actual man-hour values with the predicted values. It is noticeable that the number of hidden layers in the ANN can contribute significantly to the efficiency and reliability of the module. The result got better by increasing the number of those layers. For each case and shape of the above-plotted ANNs the accuracy, of the rate was calculated as a function of the number of hidden layers, the results are shown in Fig. 7.

By increasing the number of hidden layers, the module is giving better results. However, the usage of computing resources will increase significantly, so more time will be needed for training. This can be solved by using advanced computational methods and higher computational resources. With the size of the data used, rows, and columns, increasing the number of hidden layers after 15 is impractical as the accuracy stayed almost the same after this point.

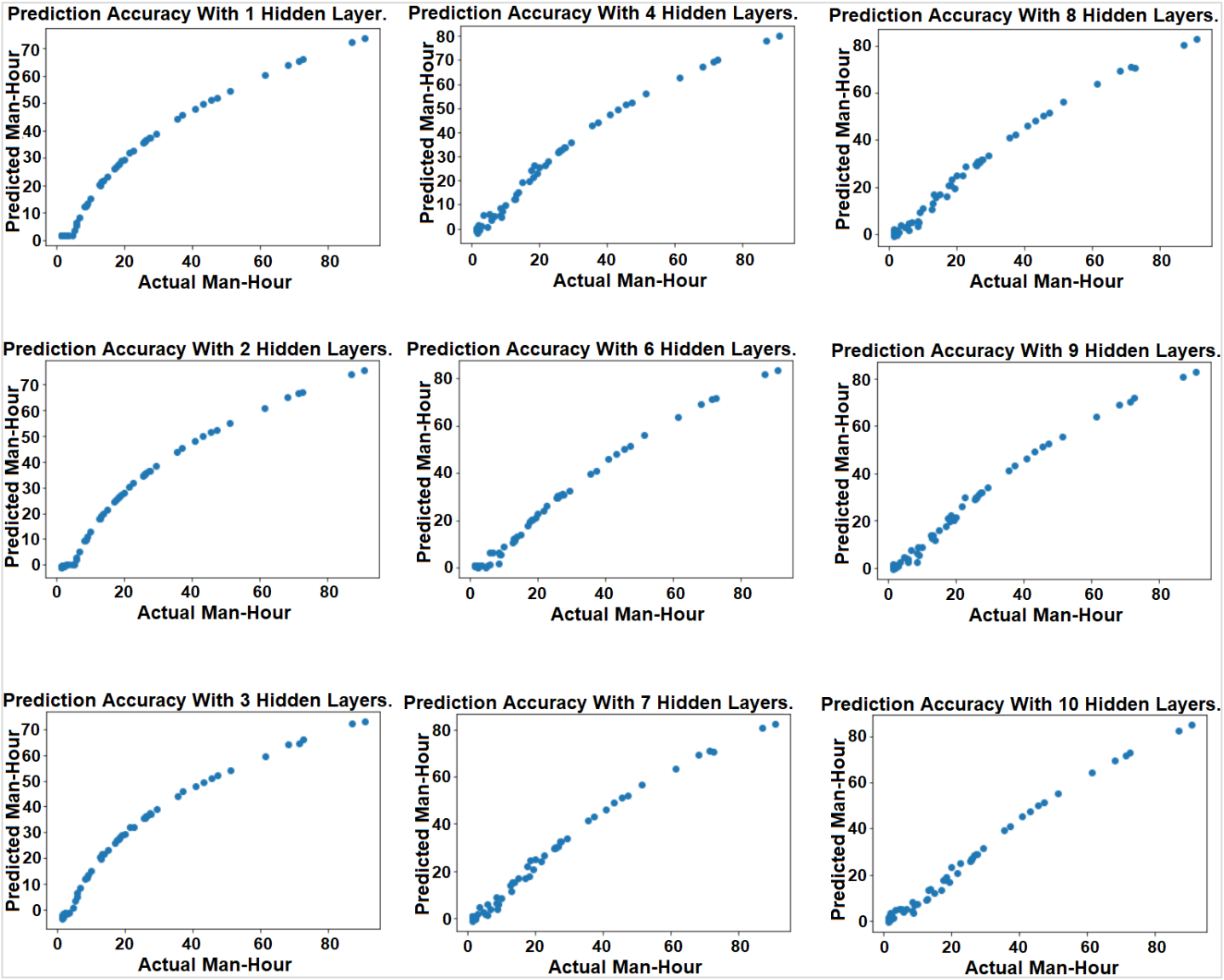

Fig. 6. Comparison between the actual man-hour and the predicted man-hour

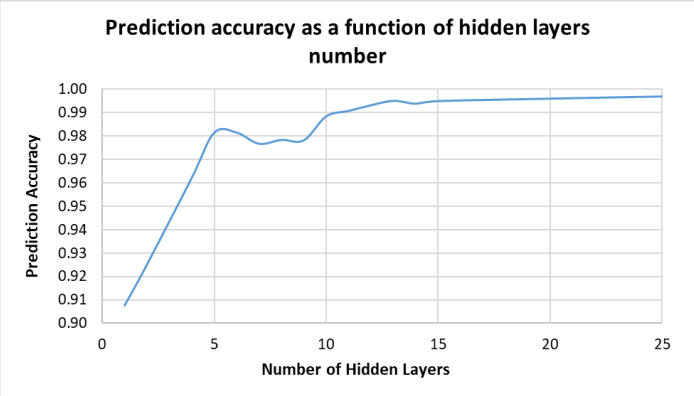

Fig. 7. Prediction accuracy as a function of hidden layers number

4. Conclusions and Future Research

Aircraft maintenance is a crucial factor in aircraft safety, reliability, and airworthiness. With the emergence of the Industry 4.0 revolution and the data era, it is logical to expect a more automated and digitalized future.

Automation and optimization of maintenance procedures go hand in hand with the advancement of AI technology. AI is the imitation of human intellectual thought processes and reasoning without the emotional aspect, which means that in the future, more and higher levels of human mistake elimination may be feasible.

Because AI comprises numerous layers and levels, it is critical to select the ideal type, form, and dimension of it to best serve the task at hand and provide value to these novel techniques.

The digitalization and the potential application of artificial intelligence in aircraft MRO processes will increase speed, improve reliability, and reduce costs by achieving predictable and consistent turnaround time (TAT). In this paper, the capabilities of neural networks for predicting the actual man hours were tested because accurate TATs lead to better aircraft release compliance and hence customer satisfaction.

The generated ANN module was capable of predicting precisely the actual tasks' man-hours for different employees and recognizing the trends based on the dummy data that we trained the ANN with. The results show that this method with minor modifications is ready to be tested on real-time data for verification and validation.

The utilization of AI in MRO operational activities will not only make planning more efficient and sustainable but also improves the utilization of company resources and enable economic operators to take on more tasks, thereby strengthening their market and competitive position and growth.

It is essential to mention that in this study, we trained and tested our ANN model for real man-hour prediction in aircraft maintenance using dummy-generated data. While dummy data allows for a controlled environment for testing and assessing model performance, it does not completely represent the complexity and variability of real maintenance duties.

We plan to use actual data in the future to verify the effectiveness of our ANN model. We can better catch nuances and variations in actual maintenance tasks, which improves the model's accuracy and generalizability.

For further work, firstly the weight of inputs will be introduced to give more accurate outputs. It assists the algorithm in determining which characteristics or factors are dominant to the job at hand. By assigning various weights to each input, the algorithm can prioritize characteristics that have a higher correlation with the intended outcome.

Another direction that could be explored is adding more input features to the module to help give more accurate results. Such features could be related to tasks such as type of the tasks (lubrication, operational test, inspection), and other features could be related to the human factor -since a lot of the inputs that are related to humans can have direct effects on the overall performance time- such features could be for example weather conditions, day or night shift, aircraft schedule (high/low season) and any other factor that could increase the model's efficiency.

For future research, the aim will be to create an interactive dashboard that integrates the appropriate AI system to aid in optimizing maintenance planning and scheduling which is going to help in visualizing the expected maintenance time length for various tasks. Future studies could include creating and testing a display like this in cooperation with maintenance specialists and end users which in return will reflect positively on the quality, cost, time, and accuracy of the MRO processes.

Nomenclature

A/C : Aircraft
AD : Airworthiness Directives
AI : Artificial Intelligence
AMP : Aircraft Maintenance Program
ANN : Artificial Neural Network
BA : Business Analytics
CBR : Case-Based Reasoning
Emp : Employee

FAA : Federal Aviation Administration

FL : Fuzzy Logic

IoT : Internet of Things

KBS : Knowledge-Based Systems

MLP : Multi-layer Perceptron

MPD : Maintenance Planning Document

MRO : Maintenance, Repair, and Overhaul

MSN : Manufacturer's Serial Number

OEM : Original Equipment Manufacturers

SB : Service Bulletins

TAT : Turn Around Time

References

Acosta, G.G., Verucchi, C.J. and Gelso, E.R. (2006) 'A current monitoring system for diagnosing electrical failures in induction motors', Mechanical Systems and Signal Processing, 20(4), pp. 953–965.

Ahmed, U., Ali, F. and Jennions, I. (2021) 'A review of aircraft auxiliary power unit faults, diagnostics and acoustic measurements', Progress in Aerospace Sciences, 124, p. 100721.

Bello, R.-W. (2016) 'Self Learning Computer Troubleshooting Expert System'.

Djenadic, S. et al. (2022) 'Risk Evaluation: Brief Review and Innovation Model Based on Fuzzy Logic and MCDM', Mathematics, 10(5), p. 811.

FAA (2011) 'Destination2025'. Federal Aviation Administration. Available at: https://www.faa.gov/about/plans_reports/media/destination2025.pdf.

FAA (2016) 'Air Carrier Maintenance Programs'. Federal Aviation Administration. Available at: https://www.faa.gov/documentLibrary/media/Advisory_Circular/AC_120-16G.pdf.

Huang, J., Chang, Q. and Arinez, J. (2020) 'Product Completion Time Prediction Using A Hybrid Approach Combining Deep Learning and System Model', Journal of Manufacturing Systems, 57, pp. 311–322. Available at: https://doi.org/10.1016/j.jmsy.2020.10.006.

Kolodner, J.L. (1992) 'An introduction to case-based reasoning', Artificial intelligence review, 6(1), pp. 3–34.

Li, J. and Lafond, D. (2023) 'Hybrid Human-AI Forecasting for Task Duration Estimation in Ship Refit', in G. Nicosia et al. (eds) Machine Learning, Optimization, and Data Science. Cham: Springer Nature Switzerland (Lecture Notes in Computer Science), pp. 558–572. Available at: https://doi.org/10.1007/978-3-031-25599-1_41.

Mate Labs (2017) Everything you need to know about Neural Networks | HackerNoon. Available at: https://hackernoon.com/everything-you-need-to-know-about-neural-networks-8988c3ee4491 (Accessed: 11 May 2022).

Moore, J. (2019) What is knowledge-based systems (KBS)? - Definition from WhatIs.com, SearchCIO. Available at: https://www.techtarget.com/searchcio/definition/knowledge-based-systems-KBS (Accessed: 9 May 2022).

Nandal, M., Mor, N. and Sood, H. (2021) 'An overview of use of artificial neural network in sustainable transport system', Computational methods and data engineering, pp. 83–91.

Pelt, M., Stamoulis, K. and Apostolidis, A. (2019) 'Data analytics case studies in the maintenance, repair and overhaul (MRO) industry', MATEC Web of Conferences, 304, p. 04005. Available at: https://doi.org/10.1051/matecconf/201930404005.

Pelt, M.M.J.M. and Stamoulis, K. (2018) 'Data Mining for Aircraft Maintenance Repair and Overhaul (MRO) Process Optimization', ISATECH 2018 [Preprint].

Pusztová, Ľ., Babič, F. and Paralič, J. (2021) 'Semi-Automatic Adaptation of Diagnostic Rules in the Case-Based Reasoning Process', Applied Sciences, 11(1), p. 292. Available at: https://doi.org/10.3390/app11010292.

Sahin, M., Kizilaslan, R. and Demirel, Ö.F. (2013) 'Forecasting aviation spare parts demand using croston based methods and artificial neural networks', Journal of Economic and Social Research, 15(2), p. 1.

Sasadmin (2014) Aircraft Maintenance Man Hour Planning Considerations • SASSofia. Available at: https://sassofia.com/blog/aircraft-maintenance-man-hour-planning-considerations/ (Accessed: 18 December 2022).

Scikit-learn (2019) Neural network models (supervised), scikit-learn. Available at: https://scikit-learn.org/0.21/_downloads/scikit-learn-docs.pdf (Accessed: 30 March 2023).

Sioson, D. (2020) 'Introduction to Fuzzy Logic', Medium, 12 August. Available at: https://medium.com/@siosond/introduction-to-fuzzy-logic-3664c610d98c (Accessed: 18 December 2022).

Xie, X. et al. (2020) 'Research on fault diagnosis of aeroengine endoscopic detection based on CBR and RBR', in Twelfth International Conference on Digital Image Processing (ICDIP 2020). International Society for Optics and Photonics, p. 115190X.

Zhou, R., Awasthi, A. and Stal-Le Cardinal, J. (2021) 'The main trends for multi-tier supply chain in Industry 4.0 based on Natural Language Processing', Computers in Industry, 125, p. 103369.

International Journal of Aviation Science and Technology

Research Article

Passive Isolator Design and Vibration Damping of EO/IR Gimbal Used in UAVs

Mehmet Taha Görmüş[1], Bilal Faruk Adın[2], Paşa Yayla[3]*

[1] Marmara University, İstanbul/Turkey
mehmettaha6060@gmail.com - 0000-0001-7332-272X

[2] Marmara University, İstanbul/Turkey
adinbilalfaruk@gmail.com - 0000-0003-0378-523X

[3] Marmara University, İstanbul/Turkey
pasa.yayla@marmara.edu.tr - 0000-0002-1787-9475

Abstract

One of the most critical factors affecting the quality of the images captured by the surveillance systems used in the unmanned aerial vehicles is the vibrations transmitted from the aircraft to the gimbal. The gimbal used in unmanned aerial vehicles is essential equipment, holding the camera steadily and accurately and pointing it in the desired direction. Within the scope of this article, a passive vibration isolation system design has been made for the two-axis electro-optical gimbal used in the mini unmanned aerial vehicle. By choosing the spring-damper system among different methods, the design that isolates the harmonic vibration from the platform on a single axis has been made using the analytical method. The analytical method was used to create a design that isolates the harmonic vibration from the platform along a single axis. In addition, the part named 'Pan Yoke', which contains this damper system, was designed with a computer-aided design program, and natural frequency values were checked with Ansys modal analysis. The frequency of the vibration transmitted from the air vehicle to the gimbal and the natural frequency of the designed part have been determined to be close to each other, at around 200 Hz. The natural frequency values of this part were optimised with various design changes and topology optimisations to prevent the part from resonating.

Keywords

Passive vibration isolators,
Harmonic vibration,
Unmanned aerial vehicles,
Ansys modal analysis,
Topology optimisation

Time Scale of Article

Received 10 January 2023
Revised until 16 May 2023
Accepted 18 May 2023
Online date 28 June 2023

1. Introduction

The primary purpose of unmanned aerial vehicles is observation. Therefore, many proper loads, such as electro-optical (EO) and infrared (IR) cameras and synthetic aperture radar (SAR) systems, are being developed worldwide for this purpose. These systems cannot fully perform their duties when exposed to vibrations originating from the environment and unmanned aerial vehicles (UAV). Many different expressions are used for similar systems around the world, such as drones, UAV, unmanned aircraft systems (UAS), and remotely controlled aircraft systems. Instead of the term drone, UAV started being used in the 1990s. In the 2010s, since the UAV only refers to the flying platform and needs at least a control station and a data link in addition to the platform for flight, UAS have started to become widespread (Karaağaç, 2016).

Although there is no common understanding after the general nomenclature is made, these aircraft are generally classified according to their various characteristics (weight, altitude, etc.). In this article, since the design of an electro-optical payload is to be mounted on an unmanned aerial vehicle that will carry

*: Corresponding Author Paşa Yayla, pasa.yayla@marmara.edu.tr
DOI: 10.23890/IJAST.vm04is01.0104

approximately 10 kg of payload and reach an altitude of 2000 meters, this aircraft will be referred to as the "mini UAV" in the article. As a result, a vibration-damping device is built inside the gimbal, which holds the cameras on the UAV body. Vibration isolation or reduction using rubber pads, steel wire, or mechanical springs is "passive vibration isolation". The passive isolators exhibit some stiffness and damping, which are critical in constructing an effective isolator. The stiffness is used to calculate the isolator's corner frequency, which is often preferred when the isolator begins isolating vibration. When determining a system's absolute transmissibility, the corner frequency (ω) is essential. For disturbances at frequencies above $\sqrt{2}$ ω, the absolute transmissibility is less than one, and vibration isolation occurs spontaneously. When the disturbance frequency is less than $\sqrt{2}$ ω, vibration amplification occurs. Absolute transmissibility is unity for disturbance frequencies much lower than the corner frequency. The isolator performs best when the disturbance frequency is greater than $\sqrt{2}$ ω. The isolator's corner frequency should be kept as low as possible. However, reducing the corner frequency too much is impossible for various reasons. One of the reasons is the spring deflection value. For example, when the system is under static loading, the isolator must dampen vibration and support the static load (Sciulli, 1997).

Before the isolator design and gimbal modal analysis, this study surveyed the literature on UAV gimbal vibration damping systems. When looking at patents for the dates when imaging systems began to be stabilised using gimbals, the 1920s (Lucian, 1923) and 1930s (Richards, 1933) are seen as early examples. Since the 1960s, various patents have been obtained for products similar to today's gimbals, both in the fields of active control (Canlong and Zhimeng, 2022) and passive vibration isolation (Leavitt et al., 1972; Tyler, 1993; Kiunke, 1993; Norén and Segerström, 1998). As we approach today, we see a complex gimbal vibration isolator design in which coils spring, elastomer, and magnetic insulators are used together in a patent obtained in 2017 (Levis, 2017). Again in 2017, it is seen that coil springs and insulators are mentioned for a large and complex gimbal (Zeise and Anderson, 2017). Another patent related to the elastomer mentioned a damper produced by moulding rubber between metal plates used as a vibration isolator (Tian and Jian, 2019). Steel wire rope and viscous damper are also used as passive vibration isolators in UAVs, as seen in a sample patent (Zhang et al., 2020).

In light of these technological solutions, it is seen that vibration-damping systems are essential in many sectors. Some damping methods in the literature are examined, and the elements used in these designs, such as spring, damper, elastomer, ring, wire and electromagnetic magnet, are investigated.

For example, in automotive, it is seen that the combination of a spring coil and a viscous damper is used in the vehicle suspension system (Kumar, 2021) and the seat system (Tewari and Prasad, 1999) to reduce the vibration reaching the driver. Elastomeric dampers are generally used to prevent the transmission of vibration generated by the internal combustion engine to the vehicle (Bursa, 2019).

One of the methods used in vibration isolation is the material referred to as “wire rope” in the literature (Balaji et al., 2017; Weimin et al., 1997). A wire rope isolator is generally used for small action camera-like systems on the quadcopter.

This study aims to re-design a lighter and novel gimbal system's vibration isolation system for a small class UAV using a spring and damper to prevent pan yoke resonance.

2. Requirements for the Design and the Methodology

For the design of the isolator, the characteristics of the vibration to which the system will be exposed should be known. Vibration data can be obtained from guidelines prepared for vibrations under various conditions (MIL-STD-810) or vibration sensors. Vibration analysis begins by plotting amplitude versus time. This is called time-domain data. These data are obtained from the various sensors. Usually, such data do not yield meaningful results, and converting them to the frequency domain is necessary.

For this article, data could be collected with accelerometers placed on a mini UAV. Thus, all random and harmonic vibration values can be obtained for that UAV. However, due to the lack of technical equipment, a general literature study was preferred to define the main vibration source for mini UAVs.

The vibration source in the aircraft can be classified into three main groups: vibrations originating from the external environment, vibrations from the propulsion system of the aircraft, and vibrations arising from other functions of the aircraft. Vibrations originating from the external environment are ground vibrations during taxi and take-off (Burström et al., 2006) and vibrations caused by aerodynamic forces during flight (Liu, 2020).

This study considers the engine as the primary vibration source in mini-UAVs. According to the design criteria obtained by examining these studies, first, the spring stiffness value and damping coefficient are calculated analytically, and then the spring design is made with these values. Then, after the spring and damper systems are designed, the pan yoke design is accomplished, the mode shapes are examined, and design changes are

made so that the gimbal does not resonate.

Since the gimbal designed within the scope of this work does not take images during the UAV's taxi, take-off, and landing phases, only the cruise phase is taken into account during the modelling of the vibration to which the optical system is exposed. During the cruise, vibrations caused by aerodynamic forces and the vibration of the UAV engine are effective. Turbulence, which an aircraft is subjected to, can be used as an example of an aerodynamic force. The damping rate of this vibration of the passenger seats is investigated in the work of Ciloglu and his co-authors on the magnitude of these vibrations at different flight stages (Ciloglu et al., 2015). However, since modelling the vibration caused by aerodynamic forces would be so comprehensive that it would be another topic, only engine-induced vibrations are examined in this article.

In the work by Lai and Jan (Lai and Jan, 2011), the effect of the engine vibration of the mini UAV on the GPS was investigated. The UAV mentioned in this work has an 80 cc two-stroke gasoline engine with a 3.5 m wingspan. Ge and his co-workers (Ge et al., 2021) found that the UAV's in-flight vibration intensities at the horizontal level were consistently higher than those in the vertical direction.

Also, according to Lai and Jan (Lai and Jan, 2011), temporal information is lost in the conversion process. However, in their study, the vibration frequency changed over time as the aircraft was operated under different flight conditions. Because of this, the short-time-Fourier transform method was used to observe the temporal information in the frequency domain, and the dominant vibration frequency at different times during the flight was determined. If the determined frequencies are examined, it can be seen that they are related to the engine speed and propeller speed and are between 100-150 Hz during the cruise.

Since the multi-rotor aircraft used in a recent work (Ge et al., 2021) and other similar studies have electric motors and many propellers, they may not show the same vibration characteristics as the piston engine and single propeller mini unmanned aerial vehicles that are the subject of this article.

The design requirements of the targeted gimbal are given in Tables 1 and 2.

Table 1. Design requirement and its physical properties

Necessary Properties	Numerical Value
Dimensions	H250 mm, W230 mm, L230 mm
Optical System Weight	1.5 kg
Gimbal Weight	< 5 kg
Yaw Angle	360°
Pitch Angle	-30°, +110°

$$Frequency\ of\ Engine = \frac{12000\ rpm}{60} = 200\ Hz$$

Table 2. Design requirement and its vibration characteristics

Characteristics of Excitation Vibration	Type and Limitation
Vibration Type	Harmonic Base Excitation
Excitation Frequency	200 Hz
Required Isolation	97%
Max Static Deflection	0.3 mm

3.Calculations

3.1. Isolation System Design Calculations

The transmissibility plot and iterations may be needed to select the correct k_{eq} and c_{eq} values for the targeted design. First, some necessary parameters can be used to understand the transmissibility graph Figure 1, and create the iteration table, Table 1.

$$\omega_n = \sqrt{\frac{k}{m}} \quad (1)$$

$$r = \frac{\omega}{\omega_n} \quad (2)$$

$$\zeta = \frac{c}{2\sqrt{km}} \quad (3)$$

After that, using the transmissibility ratio, the ratio of output to input, the right k and c values can be easily chosen.

$$\beta = \sqrt{\frac{1+(2*\zeta*r)^2}{(1-r^2)^2+(2*\zeta*r)^2}} \quad (4)$$

Moreover, static deflection can also be considered for choosing k_{eq} and c_{eq} values;

$$\delta = \frac{mg}{k} \quad (5)$$

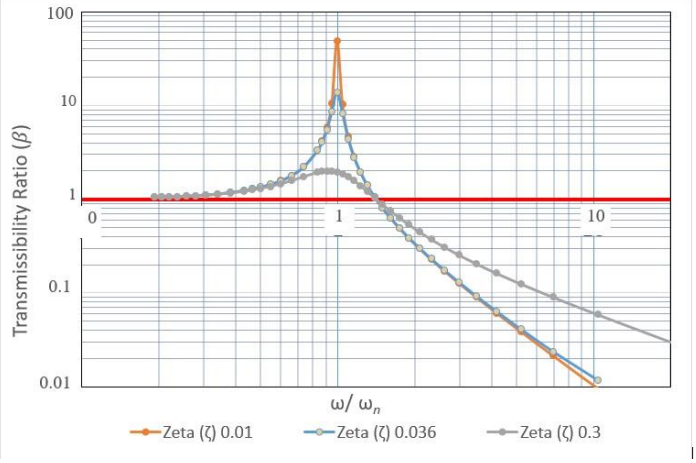

Fig. 1. Transmissibility of gimbal structural system

Firstly, the iteration can be started with m = 1.5 kg (defined earlier in the system requirements) and k_{eq} =

1000 N/m, and c_{eq} = 2 Ns/m. The iterations were executed using Excel and are listed in Table 3. The iteration was started with small k_{eq} and c_{eq} values because if it is started with large values, it may miss intermediate values smaller than the initial value. It is also seen in Figure 1 that the 0.03 transmissibility ratio for different zeta (ζ) values in Table 3 is obtained around the r-value of approximately 7.x

Figure 1 illustrates how the transmissibility value significantly rises as the r value gets closer to 1. The circumstance is known as resonance. This demonstrates that no vibration damping is used in the design and that the vibration is conveyed without damping. Different k_{eq} and c_{eq} values are introduced into the equations to produce better transmissibility and deflection values in order to avoid this problem.

The dumping coefficient employed in the system is determined using the damping ratio designated as zeta in the formulas and diagrams. Transmissibility is influenced by three elements, as shown in Figure 1. These are the system's dumping ratio, the driving frequency, and the part's inherent frequency. The (r) value must be as high as feasible for the low transmissibility to occur. On the other hand, the drive frequency is a value that operates outside and cannot be altered. Because the system's stiffness cannot be decreased below the level necessary for static strength, the natural frequency cannot be reduced to extremely low values.

Even at equal driving and natural frequencies, resonance is avoided by the large damping ratio. For values when the zeta is high, increasing the (r) value is insufficient to achieve the necessary transmissibility value. The transmissibility values derived for various damping ratios and (r) values are displayed in Figure 1 and Table 3.

Table 3. Iteration to find k_{eq} and c_{eq} values for the system

Iteration Number	k_{eq} (N/m)	c_{eq} (Ns/m)	ζ	r	β	δ (mm)
1	1000	2	0.02582	48.67	0.00114	14.715
2	10000	2	0.00817	15.39	0.00437	1.4715
3	20000	5	0.01443	10.88	0.00893	0.7358
4	30000	8	0.01886	8.89	0.01353	0.4905
5	40000	15	0.03062	7.70	0.01899	0.3679
6	50000	20	0.03652	6.88	0.02413	0.2943

The iteration can be stopped after the sixth iteration because static deflection and transmissibility values are acceptable for system requirements.

k_{eq} value is 50000 N/m and c_{eq} value is 20 Ns/m (6)

Analytical calculation of natural frequency:

$$\omega_n = \sqrt{\frac{50000}{1.5}} = 182.57 \frac{rad}{s} = 29.05Hz \quad (7)$$

3.2. Analytical Solution of Equation of Motion

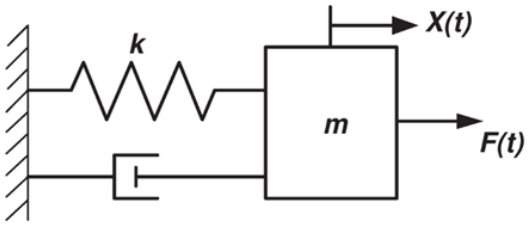

Fig. 2. A Mass- spring- damper system with external force

$$m_{eq}\ddot{x} + c_{eq}\dot{x} + k_{eq}x = F_{eq}(t) \quad (8)$$

The general solution can be written using Equation 9;

$$x(t) = x_h(t) + x_p(t) \quad (9)$$

After some requirements and iterations (k_{eq} and c_{eq}) value of these physical properties can be listed below:

$$m_{eq} = 1.5\ kg$$
$$c_{eq} = 20\ Ns/m$$
$$k_{eq} = 50000\ N/m \quad (10)$$
$$F_{eq} = 500 \sin(942.48t)\ N$$

After determining the values of properties, the homogenous solution can be solved first.

$$1.5\ \ddot{x} + 20\ \dot{x} + 50000\ x = 0 \quad (11)$$

The characteristic equation becomes:

$$1.5\ r^2 + 20\ r + 50000 = 0 \quad (12)$$

Roots can be found as follows:

$$r_{1,2} = -\frac{20}{3} \pm i\ \frac{20\sqrt{749}}{3} \quad (13)$$

Hence, the homogenous solution can be found using differential equation knowledge:

$$x_h(t) = e^{\left(-\frac{20}{3}\right)t}\left(C_1 \cos\left(\frac{20\sqrt{749}}{3}t\right) + C_2 \sin\left(\frac{20\sqrt{749}}{3}t\right)\right) \quad (14)$$

$$x_h(t) = e^{\left(-\frac{20}{3}\right)t}\left(C_1 \cos(182.452t) + C_2 \sin(182.452t)\right) \quad (15)$$

Then, the particular solution can be determined using the method of undetermined coefficients method:

$$x_p(t) = A cos(942.48t) + B sin(942.48t) \quad (16)$$

The first and second derivatives of a particular solution can be found as:

$$\dot{x_p}(t) = (-942.48)\ A\ sin(942.48t) + (942.48)\ B\ cos(942.48t) \quad (17)$$

$$\ddot{x_p}(t) = -(942.48)^2\ A\ cos(942.48t) - (942.48)^2\ B\ sin(942.48t) \quad (18)$$

The first and second derivatives can be put into the

damper-spring-mass (Figure 2) differential equation:

$$1.5\left(-(942.48)^2\, A\, cos(942.48t) - (942.48)^2\, B\, sin(942.48t)\right) + 20\left((-942.48)\, A\, sin(942.48t) + (942.48)\, B\, cos(942.48t)\right) + 50000\,(Acos(942.48t) + Bsin(942.48t)) = 500\sin(942.48t) \quad (19)$$

$cos(942.48t)$ and $sin(942.48t)$ terms are gathered separately:

$$cos(942.48t)(-1.5(942.48)^2\, A + 20\,((942.48)\, B + 50000\, A) = 0 \quad (20)$$

Roots can be found as follows:

$$sin(942.48t)(-1.5(942.48)^2\, B - 20\,\left((942.48)\, A + 50000\, B\right) = 500\, sin(942.48t) \quad (21)$$

Then the A and B coefficients can be found as:

$$A = -5.73 \times 10^{-6} \;\&\; B = -3.90 \times 10^{-4} \quad (22)$$

After that, the particular solution can be found as follows:

$$x_p(t) = -5.73\text{x}10^{-6} cos(942.48t) - 3.90\,\text{x}10^{-4}\, sin(942.48t) \quad (23)$$

The general solution can be written as follows:

$$x(t) = e^{\left(-\frac{20}{3}\right)t}\,(3.06x10^{-4}\cos(182.452t) + 0.00202\sin(182.452t)) - 5.73\text{x}10^{-6} cos(942.48t) - 3.90\,\text{x}10^{-4}\; sin(942.48t \quad (24)$$

Equation 24 can be plotted in Matlab by choosing t=0:0.01:2, as shown in Figure 3.

Figure 3 illustrates the displacement motion of the nonhomogeneous mass-spring-damper system against time. It shows the characteristic behaviour of the vibration against time and how long the vibration is damped.

4.Numerical Analysis

A bracket was designed to hold the motor connected to the shaft and springs, whose stiffness values were calculated analytically and placed between the bracket and the yoke. In addition, since the system is modelled as 1 DOF in the analytical solution, the constraints to ensure this have been considered in the design.

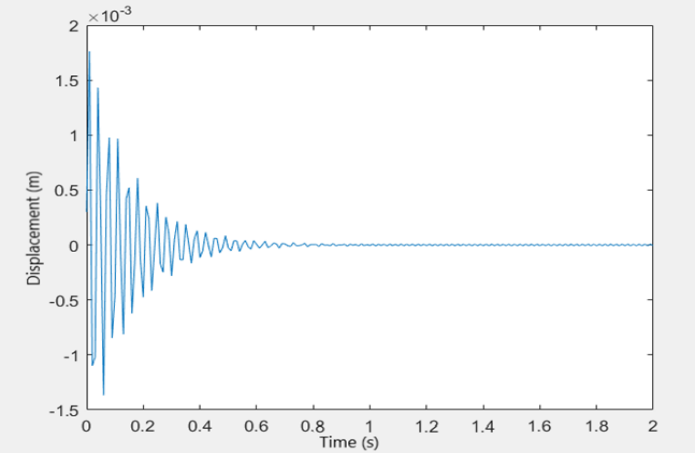

Fig. 3. Hand solution of forced vibration equation, Equation 24

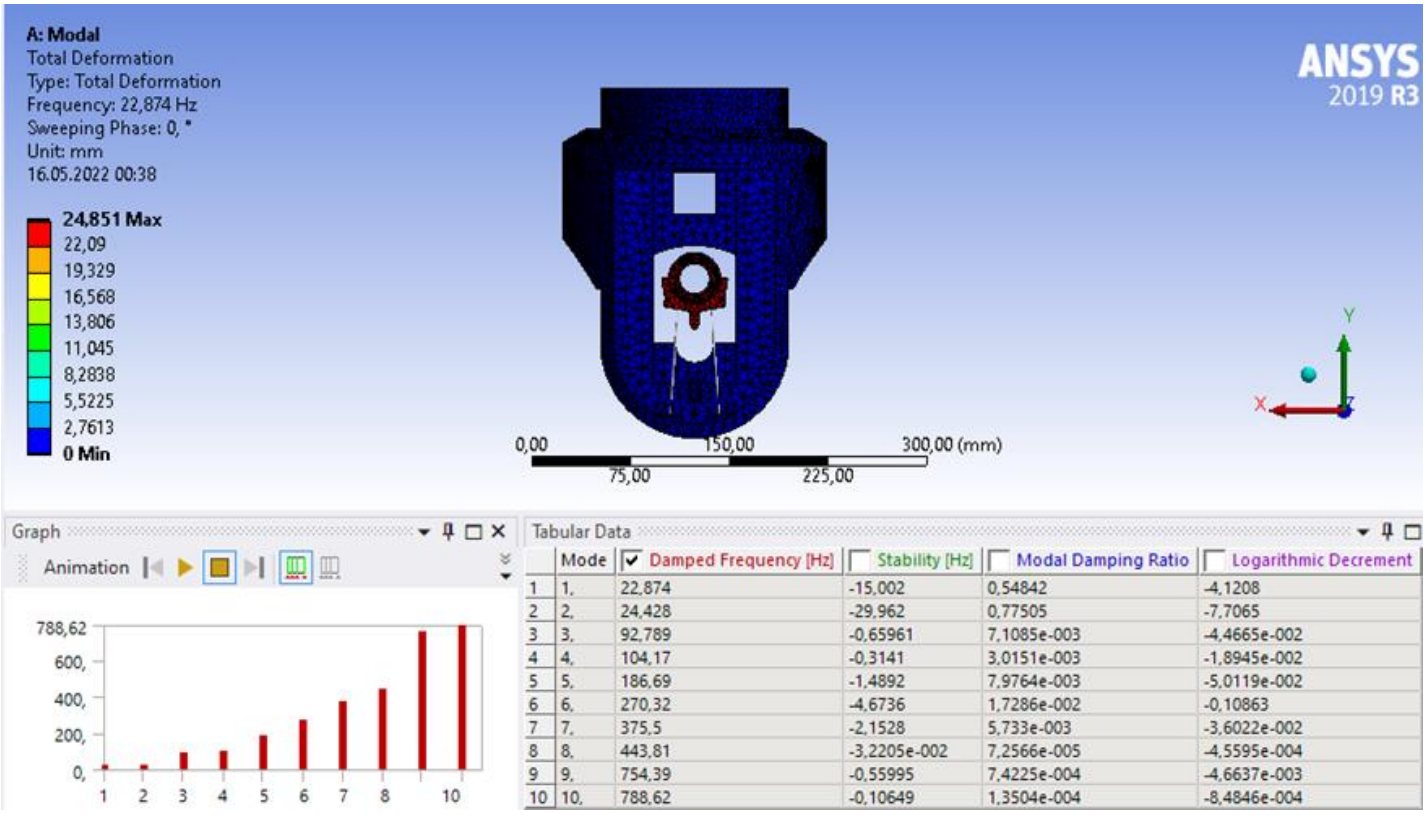

	Mode	Damped Frequency [Hz]	Stability [Hz]	Modal Damping Ratio	Logarithmic Decrement
1	1.	22,874	-15,002	0,54842	-4,1208
2	2.	24,428	-29,962	0,77505	-7,7065
3	3.	92,789	-0,65961	7,1085e-003	-4,4665e-002
4	4.	104,17	-0,3141	3,0151e-003	-1,8945e-002
5	5.	186,69	-1,4892	7,9764e-003	-5,0119e-002
6	6.	270,32	-4,6736	1,7286e-002	-0,10863
7	7.	375,5	-2,1528	5,733e-003	-3,6022e-002
8	8.	443,81	-3,2205e-002	7,2566e-005	-4,5595e-004
9	9.	754,39	-0,55995	7,4225e-004	-4,6637e-003
10	10.	788,62	-0,10649	1,3504e-004	-8,4846e-004

Fig. 4. Modal analysis results of first gimbal

The natural frequency, calculated analytically as 29.05 Hz, was found to be 22.87 Hz in Ansys (1st mode longitudinal axis of spring), as shown in Figure 4. One of the reasons for this was that the weight assumed in the analytical solution was 1.5 kilograms due to the weight of the optic ball. However, during the analysis, the motor that moves the optical system and the weight of the brackets holding these motors are added to the system. When the weight of the motors and brackets, approximately 400 grams, is considered in the analytical solution, the natural frequency is obtained as 25.81 Hz.

Sweeping phase 0 refers to the first step of the analysis, where the software calculates the static deformation of the structure due to the loads applied to it. This is also known as the "pre-stress" or "pre-load" step. During this phase, the software applies the loads to the structure and calculates the corresponding displacements and deformations. The results of this step are then used as the initial conditions for the dynamic analysis that follows.

The modal damping ratio is expressed as the ratio of the actual damping in a mode to the critical damping for that mode. Critical damping corresponds to the minimum amount of damping required for a system to return to its equilibrium position before oscillating after a disturbance. The ratio decreased in every mode.

After the static analysis, the result shown in Figure 5(a) was obtained using the Ansys topology module. Here, the objective function was chosen for topology optimisation to minimize compliance and maximize the natural frequency. Considering this result and the part's manufacturability, Figure 5(b) was designed with SolidWorks. Following this stage, the yoke's modal analysis was repeated several times, and design changes were made to increase the lowest natural frequency without significantly increasing the mass, Figure 5(c).

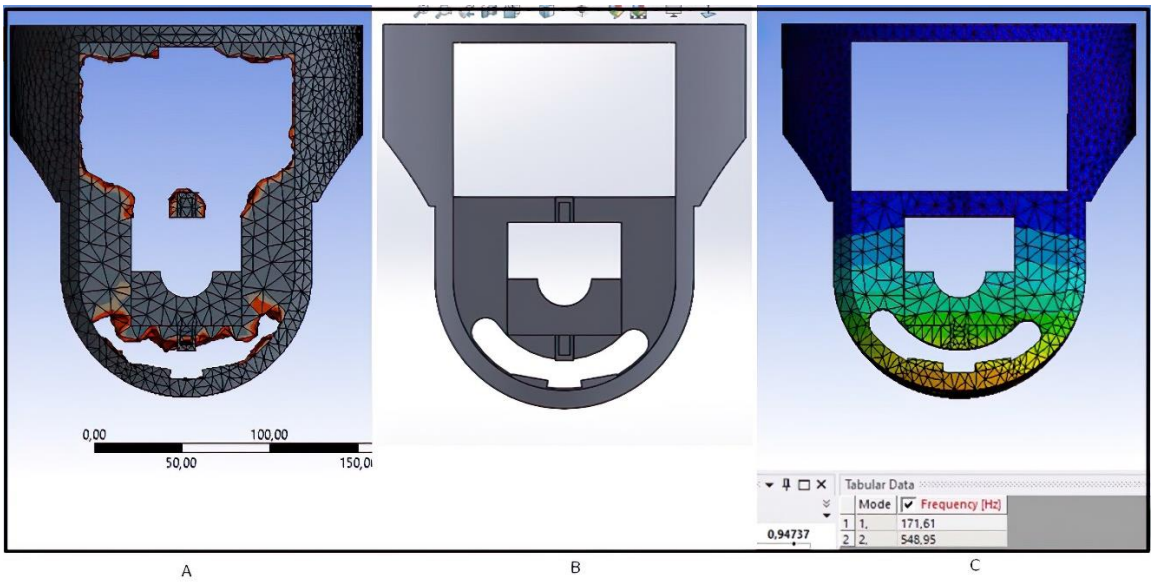

Fig. 5. Topology optimisation result (A), CAD design (B), modal analysis (C)

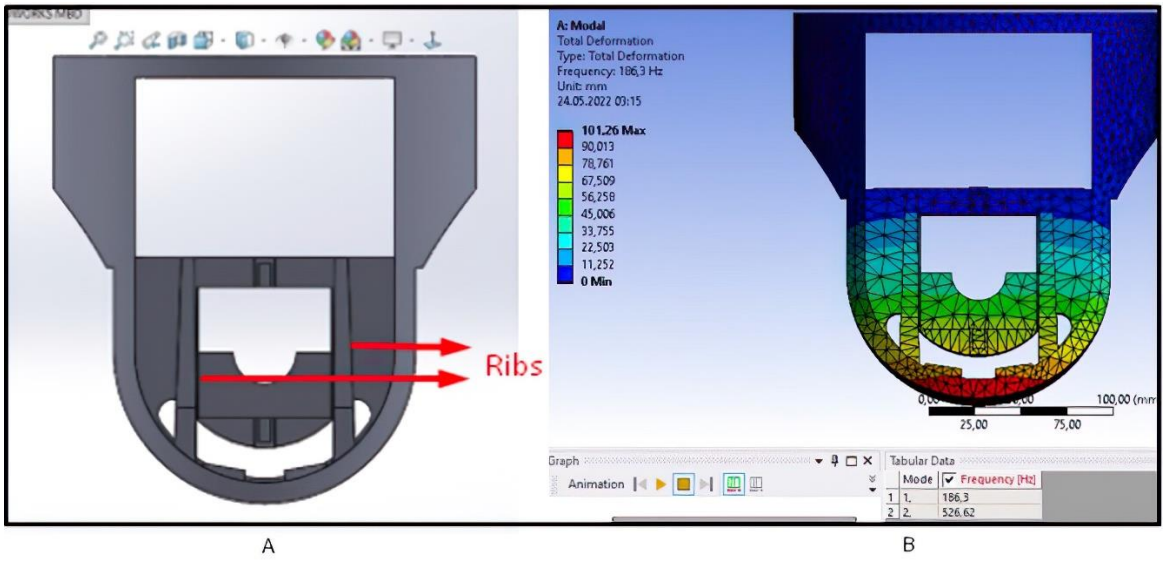

Fig. 6. CAD design with ribs (A) and its modal analysis (B)

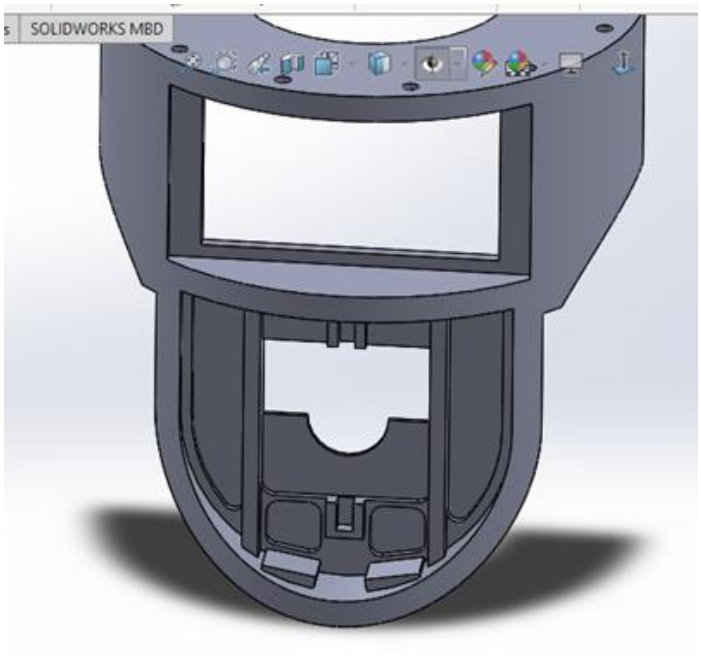

Fig. 7. Mid-section thickened design

Table 4. Effect of the mesh size on the natural frequencies

Mode	Mesh Size 7 mm Frequency (Hz)	Mesh Size 6 mm Frequency (Hz)	Mesh Size 5 mm Frequency (Hz)
1	22.673	22.673	22.673
2	24.649	24.649	24.65
3	388.24	385.91	383.35
4	474.11	472.03	468.34
5	474.12	472.14	470.49
6	540.6	538.43	535.83

After the design changes in Figures 6 and 7 were made, the final design seen in Figure 8 was obtained.

For the analysis mentioned in the design part, an average mesh size was chosen for rapid analysis. In this part of the work, the final design was analysed to see how the obtained results related to mesh quality and size. If the changes in the natural frequencies obtained by changing the mesh are small, it can be assumed that the natural frequency values will converge to a certain value.

After reaching the final design mesh size, the analysis can be executed. To accomplish this, three different mesh sizes are chosen. These mesh sizes are 7 mm, 6 mm, and 5 mm. The natural frequency values of the final design obtained with these different meshes are shown in Table 4 and Figures 9-11.

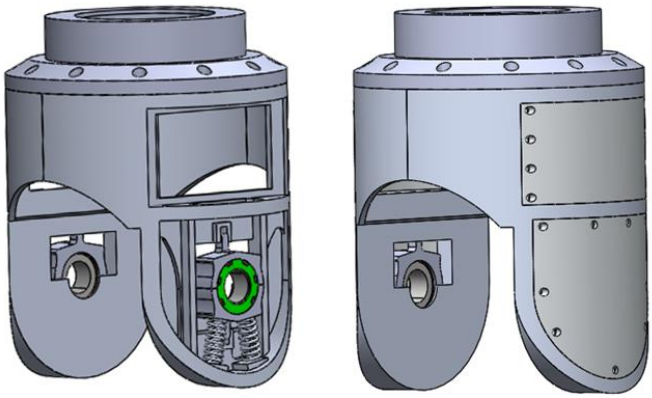

Fig. 8. Final gimbal design without cover and with cover

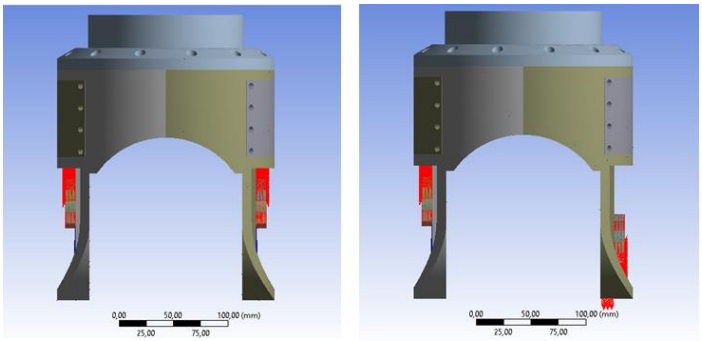

Fig. 9. First mode shape 22.673 Hz (left) and the second mode shape 24.65 Hz (right)

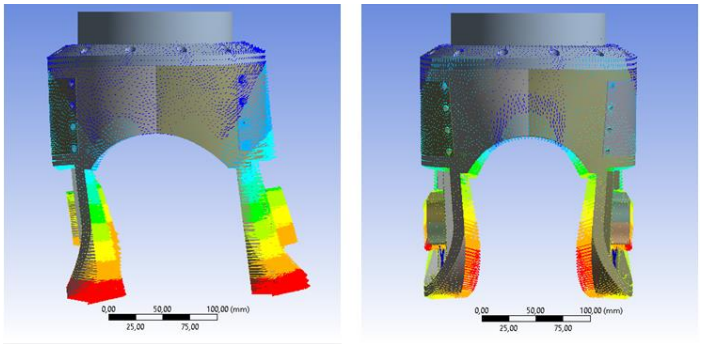

Fig. 10. Third mode shape 383.35 Hz (left) and the fourth mode shape 468.34 Hz (right)

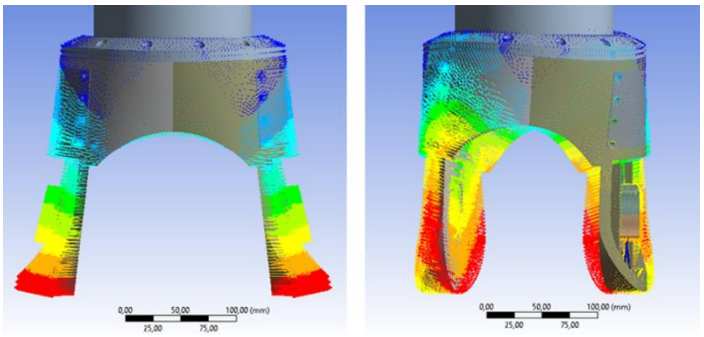

Fig. 11. Fifth mode shape 470.49 Hz (left) and the sixth mode shape 535.83 Hz (right)

5. Results and Discussions

In this study, an ideal design of a passive isolation system is obtained for the EO/IR gimbal used in mini unmanned

aerial vehicles by using the spring and damper, which are the essential mechanical isolation elements. While making this design, an iterative method is followed by using the necessary formulations for spring constant and damping coefficient selection. Then, to see the vibration damping after the k and c values were found by the iterative method, the quadratic non-homogeneous differential equation was solved by hand and plotted with Matlab.

The spring stiffness was calculated as 50000 N/m and the damping coefficient as 20 Ns/m in the design, which gave a 3% transmissibility rate for 97% vibration isolation in the design requirements.

Then the part weight is minimised with topology optimisation. After the topology optimisation, the mass was reduced by approximately 15%.

After topology optimisations, the final part design was subjected to modal analysis. Initially, the system's natural frequencies coincided with the base excitation frequency and entered a state of resonance. To prevent this, some changes in the design of our piece were made. For example, adding a rib moved the natural frequency values away from the base excitation frequency value.

- The third natural frequency increased from 92.8 Hz to 388.4 Hz.
- The fourth natural frequency increased from 104.2 Hz to 468.3 Hz.
- The fifth natural frequency increased from 186.7 Hz to 470.5 Hz.

After reaching the desired natural frequency values, the analysis was performed in 3 different mesh sizes (5 mm, 6 mm, and 7 mm) to observe the effect of mesh size on the results.

- A difference of less than 1% was observed in the frequency results obtained when the mesh number was increased.

6. Conclusions

This study presents a lighter and novel passive isolator system and gimbal design, considering the vibration that the gimbal in a mini unmanned aerial vehicle is exposed to and validated with modal analysis. It is revealed where the vibration originates, how it can be dampened, and how the design can be altered to prevent resonance in the system.

With this study, a novel design of a passive isolation system is obtained. Following topological optimization, the mass of the passive isolator was decreased by 15% or such.

In future studies, more realistic results can be obtained from the harmonic vibration assumption considered in the current work by experimentally performing vibration measurement and spectrogram analysis on the UAV. Afterwards, the analyses were made with a CAD design in which all optics and electronic parts, even nuts and gaskets, are modelled in the gimbal and can be more helpful in determining the natural frequencies and mode shapes. Finally, as it may yield more realistic results, choosing a system with multiple degrees of freedom rather than a single one is possible.

Acknowledgement

The authors would like to thank TÜBİTAK for supporting the work within the scope of the 2209-A University Students Research Projects Support Program, which provides financial support. The technical support provided by Blitz Systems is also well appreciated.

CRediT Author Statement

Mehmet Taha Görmüş: Investigation, Conceptualization, Methodology, Analysis, Original draft preparation. **Bilal Faruk Adın**: Investigation, Conceptualization, Methodology, Analysis, Data curation, Writing- Original draft preparation. **Paşa Yayla**: Supervision, Investigation, Conceptualization, Methodology, Writing- Reviewing and editing.

References

Balaji, P. S., Moussa, L., Khandoker, N., Shyh, T. Y., Rahman, M. E. and Ho, L. H. (2017) 'Experimental study on vertical static stiffnesses of polycal wire rope isolators', In IOP Conference Series, Materials Science and Engineering, 217(1): p. 012032), IOP Publishing. doi:10.1088/1757-899X/217/1/012032

Bursa, A.İ. (2019) 'Vibration Transmission Investigation of Engine Mounting Brackets', MSc Thesis, İTÜ, Institute of Science and Technology, Istanbul-Turkey, (In Turkish).

Burström, L., Lindberg, L., and Lindgren, T. (2006). Cabin attendants' exposure to vibration and shocks during landing. Journal of Sound and Vibration, 298(3), 601-605. https://doi.org/10.1016/j.jsv.2006.06.026

Canlong, L. and Zhimeng, S. (2022) 'Control methods, apparatus, and device, and UAV', United States, Patent No. US11216013B2, (2022).

Ciloglu, H., Alziadeh, M., Mohany, A. and Kishawy, H. (2015) 'Assessment of the whole body vibration exposure and the dynamic seat comfort in passenger aircraft', International Journal of Industrial Ergonomics, 45, pp. 116-123. doi:10.1016/j.ergon.2014.12.011

Ge, C., Dunno, K., Singh, M. A., Yuan, L., and Lu, L. X.

(2021). Development of a drone's vibration, shock, and atmospheric profiles, Applied Sciences, 11(11), 5176. doi:10.3390/app11115176

Karaağaç, C. (2016). İHA Sistemleri Yol Haritası Geleceğin Hava Kuvvetleri 2016-2050. STM-Mühendislik Teknolojik Danışmanlık, retrieved from https://thinktech.stm.com.tr/uploads/docs/1608914423_satm-bb-17-0200-sektor-raporlari-iha-260417.pdf

Kiunke, P.C. and Schaefer, R. D. (1993) 'Gimbal vibration isolation system', European Patent Office, Patent No. EP0559402A2, (1993).

Kumar, D. (2021) 'Durability analysis of helical coil spring in vehicle suspension systems', PhD Thesis, Virginia Tech., USA.

Lai, Y. C. and Jan, S. S. (2011) 'Attitude estimation based on fusion of gyroscopes and single antenna GPS for small UAVs under the influence of vibration', GPS Solutions, 15(1), pp. 67-77. doi:10.1007/s10291-010-0171-y

Leavitt, J.N., Alas, R. and Dafoe, E.C. (1972) 'Stabilized camera mount' United States, Patent No. US3638502.

Levis, M.D. (2017) 'Platform stabilisation system', United States, Patent No. US9765925B2.

Levis, M.D. (2001) 'Stabilized platform systems for payloads', United States, Patent No. US6263160.

Liu, Y. (2020). Study on the vibrational comfort of aircraft in formation flight. Aircraft Engineering and Aerospace Technology, 92(8), 1307-1316. doi.org/10.1108/AEAT-12-2018-0311

Lucian, A.N. (1923) 'Stabilizer', United States, Patent No. US1634950.

Norén, K. and Segerström, T. (1998) 'A Device for stabilizing of a remotely controlled sensor, like a camera', European Patent Office, No: WO1998016871A1.

Richards, W.H. (1933) 'Universal camera mount', United States, Patent No. US1955770.

Sciulli, D. (1997) 'Dynamics and Control for Vibration Isolation Design' PhD Thesis, Virginia Polytechnic Institute and State University, USA.

Tewari, V. K. and Prasad, N. (1999) 'Three-DOF modelling of tractor seat-operator system", Journal of Terramechanics, 36(4), pp. 207-219. doi:10.1016/S0022-4898(99)00008-7

Tian, Y. and Jian, W. (2019) 'Gimbal vibration damper for UAVS', United States, Patent No. US10260591B2.

Tyler, N. (1993) 'Gyroscopically stabilized apparatus', United States, Patent No. US5184521A.

Weimin, C., Gang, L. and Wei, C. (1997) 'Research on ring structure wire-rope isolators', Journal of Materials Processing Technology, 72(1); pp. 24-27. doi:10.1016/S0924-0136(97)00124-6

Zeise, S.W., and Anderson, R.D. (2017) 'Gimbal system having preloaded isolation', United States, Patent No. US2017175948A1.

Zhang, S., Zhang, Y. and Liang, G. (2020) 'Damping device, gimbal assembly having same, and unmanned aerial vehicle', United States, Patent No. US2020307826A1.

International Journal of Aviation Science and Technology

Research Article

The Detection Capability of Laser Fuze in Fog, Mist, and Haze Using Monte Carlo Simulations

Hoang Linh Nguyen[1],Trung Dung Pham[2],Chung Thanh Nguyen[3],Hong Son Tran[4]*

[1] *Faculty of Control Engineering, Le Quy Don Technical University, 100000 Hanoi, Vietnam*
nghoanglinh86@gmail.com - 0000-0002-2041-6383
[2] *Faculty of Control Engineering, Le Quy Don Technical University, 100000 Hanoi, Vietnam*
thchdung@gmail.com - 0000-0003-1812-3642
[3] *Faculty of Control Engineering, Le Quy Don Technical University, 100000 Hanoi, Vietnam*
nguyenthanhchung@lqdtu.edu.vn - 0000-0003-1182-8746
[4] *Faculty of Control Engineering, Le Quy Don Technical University, 100000 Hanoi, Vietnam*
tranhongson@lqdtu.edu.vn - 0000-0002-7956-2377

Abstract

When choosing a laser wavelength for proximity fuze with high accuracy requirements, the weather condition is a considerable element. Hence, the paper developed a laser detection model in different conditions based on the Monte Carlo method to evaluate the detection capability. As the atmospheric attenuation is a function of the wavelength, there is a conception that the laser pulsed fuze with 1550 nm light suffers from less atmospheric attenuation than 785 or 850 nm laser in all weather conditions (Pratt, 1969). However, in foggy weather (visibility <500 m), the results showed that laser attenuation appeared to be wavelength independent, i.e. the wavelengths of 785 nm, 850 nm, and 1550 nm are equally all attenuated equally by fog. Furthermore, the simulations also allowed the prediction of transmission, as well as the effects of energy scattering and absorption. This paper can provide guidance and reference for the application of laser wavelengths in the laser fuze.

Keywords

Atmospheric attenuation,
Laser pulse fuze,
Monte Carlo,
Detection capability

Time Scale of Article

Received 15 December 2022
Revised to 27 April 2023
Accepted 29 April 2023
Online date 28 June 2023

1. Introduction

A laser fuze is a weapon component using lasers to identify close-range targets, often at a distance of fewer than 20 meters, and regulates the time of ammunition explosion depending on the information from the identified targets (Hu et al., 2017). However, the near-infrared spectrum, which almost laser fuze output wavelengths presently utilize, is significantly influenced by the bad atmosphere (Liu, 2017). In contrast to radio wavelengths, optical wavelengths correspond to particles of the same size as vapor; consequently, atmospheric phenomena such as cloud, fog, and haze scatter laser beams (Kavehrad and Hamzed, 2005). The key optical phenomena which influence the detection performance of laser fuze in cloudy conditions are scattering, absorption and reflection. The absorption and scattering of the clouds reduce the energy of the signal reflected from the target in clouds, making it hard for the fuze to detect the target. The detection capabilities of the laser fuze are therefore assessed using parameters that take into account light propagation in cloudy environments. A simulation of the photon path through different weather conditions has been proposed from the three primary optical processes.

Fog, mist, and haze are visibility types in the cloud medium. A cloud is generated when water vapor from evaporation toward the sky and condenses at high altitudes. Clouds arise when vapor condenses around dust and smoke particles. Fog originally emerged when there is a lot of moisture in the air, wind, and a stable atmosphere. Haze, on the other hand, is a collection of aerosols that have been discharged into the air, such as

*: Corresponding Author Hong Son Tran, tranhongson@lqdtu.edu.vn
DOI: 10.23890/IJAST.vm04is01.0105

dust, smoke, or salt particles. Photon is absorbed and scattered by various aerosols and gaseous molecules in the atmosphere.

A current transmitter with a laser pulse electronics in proximity fuze use diode bars operating in the wavelength region from 780 to 860 nm. The wavelength and power may also be regulated by the safety class required. However, the most powerful semiconductor lasers can be found in the wavelength range of 800-900 nm. The semiconductors are GaAs, GaAlAs or InGaAs and operate over wavelength range of 850 to 910 nm. Lasers with a small output power (1 mW – 50 mW), small size, and long wavelength (1300 – 1550 nm) can be used in pulsed TOF laser fuze. These lasers use a Nd: YAG crystal as a lasing medium, and also operate in the near-infrared range, 1550 nm.

Concerning the echo signal in clouds, Wang et al. investigated the transmittance of near-, mid-, and far-infrared lasers in aerosols and discovered that the latter had higher transmittance than the former (Wang et al., 2013). The lasers used are typically in the near-infrared spectrum, as many mediums are relatively transparent at these wavelengths (Sato et al., 2002). Because of their efficiency and light weight, diode lasers are the most commonly used, though Nd:YAG and fiber lasers are also used (Kagan et al., 2002). Although they are created by the combined effects of the laser transmittance, scattering, and target reflection in clouds, target echoes in clouds are calculated just only on the transmittance. Winker and Poole simulated the cloud backscattering echo for near-infrared lidar in relation to this phenomenon (Winker and Poole, 1995). By using a near-infrared lidar, Chudamani et al. evaluated the backscattering cross-section of tropospheric aerosols (Chudamani et al., 1996). The backscattering coefficients of aerosols that resemble clouds were theoretically calculated by Srivastava et al. using near- and far-infrared lidars (Srivastana et al., 1992). Because the conclusions of these studies are all about long detection distances (generally a few hundred meters to several hundred kilometers), they are inapplicable for laser fuze with short detection ranges.

The echo energy in the presence of the target and transmission of the laser can be used as a parameter for evaluating the detection capability of laser fuze in visibility conditions. The echo energy is influenced by the attenuation coefficient. While the transmission of a laser beam is absorbed and dispersed by air molecules, suspended dust, and aerosols as it travels through the atmosphere. The purpose of the paper is to develop a model to evaluate the ability of a laser fuze to detect the target through a cloudy environment. A model based on Monte Carlo Ray Tracing (MCRT) is presented to study light passing through a scattered medium. A cloud medium is a scattering medium containing aerosols and particles, such as smoke, raindrops, etc. A photon will collide with the cloud particle when it propagates in clouds. For the photons that are returned and received successfully by the laser receiver, the energy and moment at which they are received are recorded. This direct simulation approach has the advantage of allowing for highly flexible computations, but this method needs a huge amount of computation. Because it is a statistical technique, it is necessary to calculate a large number of photons to reduce the variance in the results.

Although the model described here was designed to investigate a variety of optical effects on space-based photons, it is quite general and can be applied to a wide range of problems. The model can explain how scattering and absorption parameters (μ_{sca}, μ_{abs}) affect distance measurement. The model can estimate energy transmission and absorption, as well as a total reflection at the target surface, in order to construct a model for predicting light propagation through clouds and analyzing the detecting capabilities of the laser fuze. A successful model would allow its predictions to be used to assess the accuracy of measurements.

2. Methods

A detection model is built using the Mie scattering theory and the Monte Carlo method. In Figure 1, a coordinate system is established, with the laser emission window as the origin and the axial direction of the emitted laser as the z-axis. The technique uses a Monte-Carlo approach to generate photons through the atmospheric paths, counting for absorption, scattering and reflection from the target surface. The laser energy is represented by the number of photons. The atmospheric effects limit the capabilities of laser fuze since the laser pulse travels through the air, and some of the energy is absorbed and scattered by atmospheric molecules and suspended dust and aerosols.

2.1 Photon Positioning and Initial Conditions

In this paper, the term "photons" used in this simulation is not equivalent to photons found in particle physics, which represent a conceptual unit of light in the simulation. Each photon in the simulation is given a weight, denoted by w. Each photon began by pointing directly into the cloudy environment, where each photon began with a random, forward angle. Each photon moves along a random path length, absorbing a fraction of its weight along the way. The scattering direction is updated after each step randomly. When the laser transmitter emits photons, the initial energy of photons is $w = 1$. As the photon propagates through the atmospheric cloudy paths, it slowly loses weight at each scattering event. To prevent photons from continuing indefinitely, the photon is removed when its weight falls below a certain threshold.

A photon has three related properties: position, direction, and weight. The position of a photon is specified using three Cartesian coordinates: x, y, and z. The direction of propagation of the photon is specified using the direction cosine (u_x, u_y, u_z) to determine the photon's next position. Each photon is positioned with the same initial position of the block, denoted by x_0, y_0 and z_0. The relevant expression is:

$$x_0 = \frac{X_0}{2}, y_0 = \frac{Y_0}{2}, z_0 = 0 \quad (1)$$

For this simulation, each photon is assumed to have the same initial direction, and is perpendicular to the target surface:

$$u_{x0} = 0, u_{y0} = 0, u_{z0} = 1 \quad (2)$$

The photon moves through the clouds by taking a step in the direction currently traveling. It starts by walking along the z-axis with a random step size.

2.2 Atmospheric Transmission

Transmission is the process of propagating radiation through a cloud. It is the ratio of transmitted radiation to total radiation incident upon the cloud, measured as transmittance. Transmission in the atmosphere varies with wavelength. The scattering coefficient is wavelength dependent due to scattering across the dust and aerosol particle size distribution. The type of scattering depends on the size of the specific air particle about the transmission of wavelength.

Anisotropy, absorption, and scattering coefficients all affect transmission. This produces an attenuation of the beam power with respect to the transmitted distance, as indicated by the Beer-Lambert law. Assuming a constant atmospheric extinction coefficient, the law is as follows:

$$T_a = \exp(-\mu_{ext} Z) \quad (3)$$

Where, T_a is the one-way attenuation factor, μ_{ext} is atmospheric extinction coefficient in (mm^{-1}), and Z is range. An expression for μ_{ext}, which can be derived from the definition of visibility R_v and wavelenght λ, can be determined from experimental data, resulting in (Kruse et al., 1962):

$$\mu_{ext} = \frac{3.91}{R_v}\left(\frac{\lambda}{0.55}\right)^{-q} \quad (4)$$

Where, q is the size distribution of the scattering particles. The value of q is a function of the visibility, size, and distribution of the scattering, as determined by experimental observations and theoretical computations (Kim et al.,). Which is expressed by $q = 0.16\,R_v + 0.34$ for haze visibility (1 km $< R_v <$ 6 km), $q = R_v - 0.5$ for mist visibility (0.5 km $< R_v <$ 1 km) and $q = 0$ for fog visibility ($R_v < 0.5\ km$).

The photon moves a step in the direction to propagate through the clouds. Wilson et al. selected the step size to be random such that:

$$\Delta s = -\frac{ln\xi}{\mu_{ext}} \quad (5)$$

Where, ξ denotes a uniform random number on [0,1], and μ_{ext} is the extinction coefficient. If the weight of the photon after the collision is still greater than a threshold weight value (w_t), the photon will continue to propagate in the new direction with a distance between the two collisions equal to a photon step.

2.3 Photon Absorption

At the end of each step, some of the photon's weight is absorbed in the new position. The photon's current position is placed within the absorption matrix Q. The fraction of the photon's current weight that is lost at each step by [10]:

$$Q(i,j,k) = Q(i,j,k) + w\left(\frac{\mu_{abs}}{\mu_{ext}}\right) \quad (6)$$

Here, i, j and k represent the indices corresponding to the photon's current position. The photon's remaining weight is given by:

$$w' = \left(1 - \frac{\mu_{abs}}{\mu_{ext}}\right).w = \frac{\mu_{sca}}{\mu_{ext}}.w \quad (7)$$

2.4 Photon Scattering

The photon direction changes due to scattering off after a partial absorption event. Figure 1 shows an azimuth angle φ_{sca} in the X-Y plane and a deflection angle θ_{sca} along the Z-axis. Because scattered radiation is considered to be unpolarized, the azimuth direction is chosen to lie with equal probability on [0, 2π]. The scattering phase function φ_{sca} is expressed as

$$\varphi_{sca} = \xi.2\pi \quad (8)$$

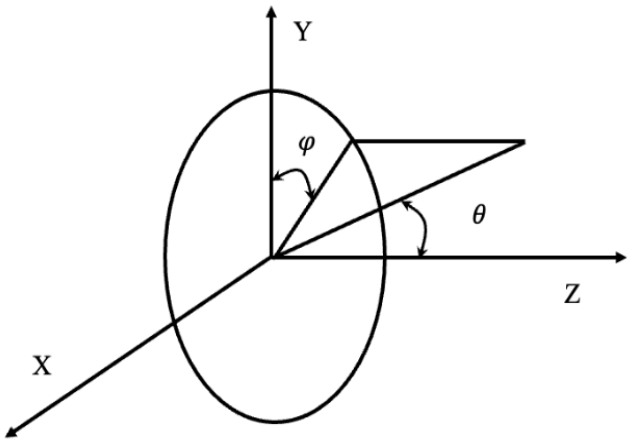

Fig. 1. Coordinate system showing azimuth and deflection angle definitions

The deflection angle θ_{SCA} defines forward (or backward). However, it is not easy to estimate a phase angle using the Mie solutions, nor to take into consideration the many sizes and shapes of particles that could be present in a single environment. The Henyey-Greenstein (HG)

function provides an approximate Mie solution (Prahl et al., 1989). The "phase problem" is roughly solved using this function in this context. To get the deflection angle, the HG phase function is adjusted (Welch and Gemert, 1995):

$$cos\theta_{SCA} = \left(\frac{\left(1+g^2-\left(\frac{1-g^2}{1-g+2g\xi}\right)^2\right)}{2g} \right) \quad (9)$$

Where g is the anisotropy factor. The anisotropy factor influences the next direction following a scattering event: forward or backward. It can vary from -1 to 1. A value g = 0 implies that scattering is completely isotropic. Transmission is higher for forward scattering ($g \rightarrow 1$) because photons are less likely to be considerably dispersed away from their original direction along the Z-axis into the clouds. As $g \rightarrow 0$, isotropic scattering increases, and the photon has a larger chance of being dispersed in any direction.

The position is determined by the angles the photon trajectory makes with each of the three Cartesian axes (u_{xx}, u_{yy}, u_{zz}). Before moving on to the next step, the trajectory of photons is updated. The direction of photon propagation is calculated by (Ilie et al., 2007):

$$\begin{cases} u_{xx} = \frac{\sin\theta_{SCA}}{\sqrt{1-u_z^2}}(u_x u_z \cos\varphi_{SCA} - u_y \sin\varphi_{SCA}) + u_x \cos\theta_{SCA} \\ u_{yy} = \frac{\sin\theta_{SCA}}{\sqrt{1-u_z^2}}(u_y u_z \cos\varphi_{SCA} + u_x \sin\varphi_{SCA}) + u_y \cos\theta_{SCA} \\ u_{zz} = -\sin\theta_{SCA}\cos\varphi_{SCA}\sqrt{1-u_z^2} + u_z \cos\theta_{SCA} \end{cases} \quad (10)$$

In the case where $u_z \cong \pm 1$ hay $|u_z| > 0.999$, the denominator of the u_{xx} and u_{yy} direction cosines becomes zero. The new direction cosines can be calculated using:

$$\begin{aligned} u_{xx} &= \sin\theta_{SCA}\cos\varphi_{SCA}, \\ u_{yy} &= \sin\theta_{SCA}\sin\varphi_{SCA}, \\ u_{zz} &= u_z/|u_z| . \cos\theta_{SCA} \end{aligned} \quad (11)$$

Where (u_x, u_y, u_z) is the direction of photon propagation before collision. Consequently, the photon moves to a new location (x', y', z'). With a step size Δs, the photon's position (x, y, z) is updated accordingly:

$$x' = x + u_{xx}.\Delta s,\ y' = y + u_{yy}.\Delta s,\ z' = z + u_{zz}.\Delta s \quad (12)$$

The photon will repeat the process of colliding with the cloud particles and scattering if its new location remains inside the cloud. The collision-propagation cycle continues until it leaves the cloud or the energy is below the threshold. Figure 2 shows the change in the propagation direction of the photon after the collision.

As the photon travels through the cloudy medium, the weight of the photon is gradually reduced with each collision event. In addition, since only a random small amount of the photon weight is removed rather than an absolute amount removed after each interaction, it is difficult to continuously track the photon weight down to zero. Therefore, the paper proposes to use an approximation. Here, the used photon weight threshold (w_t) is usually chosen as 10^{-4}. When the weight of a photon is below this threshold, it is discarded and a new photon is launched.

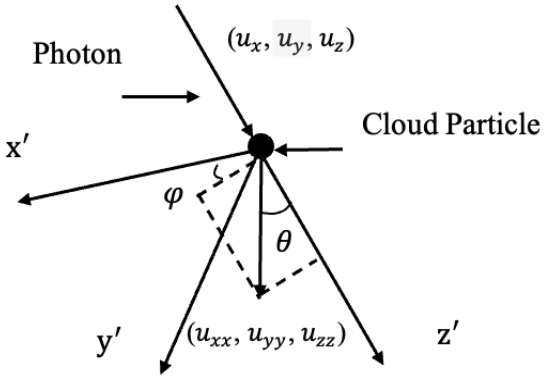

Fig. 2. Change of photon propagation direction after collision

2.5 Target Reflection

When a photon encounters a target during propagation, it is reflected by the target surface. The new direction is reversed by changing the sign of the appropriate direction angle, with no change in photon weight. Figure 3 depicts the change direction of photon propagation.

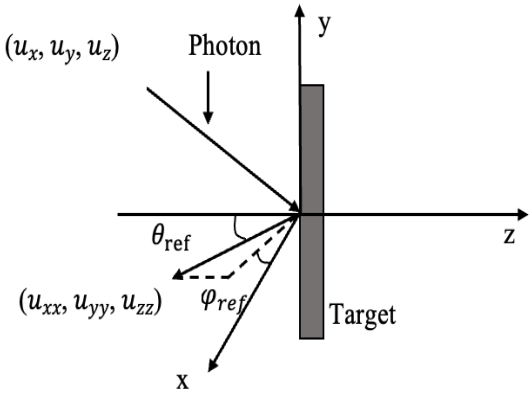

Fig. 3. Change of photon propagation direction after target reflection

3. Simulation Results and Discussion

The simulation in this paper uses the Monte-Carlo approach to generate a statistical distribution from a single point source traveling through the cloudy medium. Figure 5 shows the technique as a flowchart. At each step, the photon deposits a portion of its energy. Each step direction and duration are chosen at random, with the likelihood of a particular direction or length being defined by the simulation input parameters. Reflections at the target surface, as well as the likelihood

of their removal from the simulation, are taken into account.

The geometry of the simulation is established. The program simulates a block of light-scattering plastic in space, so here its dimensions are defined as X_0, Y_0 and Z_0, in millimeters, and the respective resolutions Δx, Δy and Δz are chosen such that.

The simulation's geometry has been established. Because the program simulates a block of light-scattering plastic in space, its dimensions are defined as X_0, Y_0 and Z_0, in millimeters, and the resolutions Δx, Δy and Δz are chosen so that

$$N_x = \frac{X_0}{\Delta x}$$
$$N_y = \frac{Y_0}{\Delta y} \quad (13)$$
$$N_z = \frac{Z_0}{\Delta z}$$

where N_x, N_y and N_z are integers representing the number of bins along each of the Cartesian direction. These numbers can vary from the tens, for low resolution cases, into the hundreds or thousands, depending on the accuracy required. These bins are used to record partial absorption by the material as photons are scattered. A matrix, labeled Q, with dimensions N_x, N_y and N_z is used to represent the block.

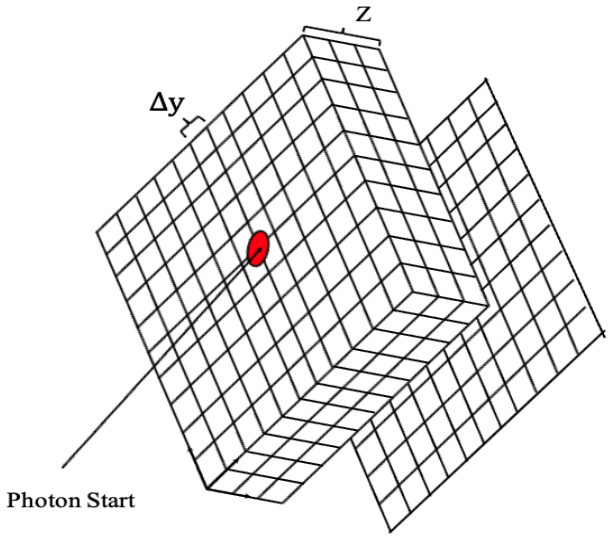

Fig. 4. Simulation block concept diagram matrix Q

With a step size chosen, the position of photon is updated accordingly to Equation (12).

As the direction of the photon has not yet been updated from the initial condition, the first step, though of variable length, is always perpendicular to the XY plane, along Z into the clouds. At every step, the position is checked to verify the photon in the cloud. For the case of a photon exceeding the target surface:

$$x_{new} = x_{current} - ux * \Delta s$$
$$y_{new} = y_{current} - uy * \Delta s \quad (14)$$
$$z_{new} = z_{current} - uz * \Delta s$$

With the photon at its previous position, the exact size of a step to the boundary along the current direction is calculated. Continuing with the case of a photon approaching the surface:

$$\Delta s_{target} = \left|\frac{z_{new}}{uz}\right| \quad (15)$$

The position is updated to bring the photon exactly to the Z surface:

$$x_{target} = x_{target} + ux * \Delta s_{target}$$
$$y_{target} = y_{target} + uy * \Delta s_{target} \quad (16)$$
$$z_{target} = z_{target} + uz * \Delta s_{target}$$

The direction of the reflected photon:

$$u_{xx} = \sin\theta_{ref}\cos\varphi_{ref}, \quad u_{yy} = \sin\theta_{ref}\sin\varphi_{ref},$$
$$u_{zz} = \cos(\pi - \theta_{ref}) \quad (17)$$

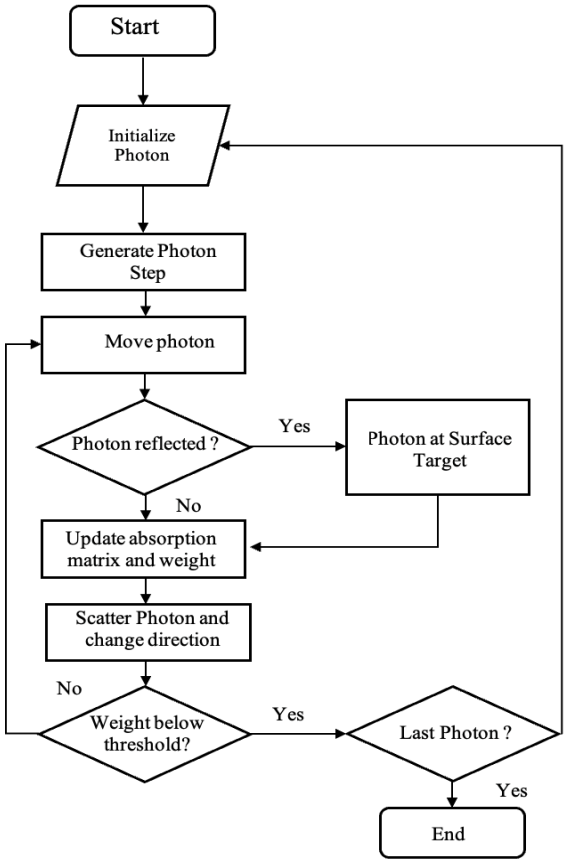

Fig. 5. Flowchart summary of the Monte Carlo Method for Photon Transport in Clouds

In this case, $z_{target} = Z_0$. There is a case of target reflection and all of the photon is returned. The direction is reversed, simply by switching the sign of the appropriate directional cosine.

$$x = x_{target} - u_{xx}.(\Delta s - \Delta s_{target})$$
$$y = y_{target} - u_{yy}.(\Delta s - \Delta s_{target}) \quad (18)$$
$$z = z_{target} - u_{zz}.(\Delta s - \Delta s_{target})$$

Furthermore, the number of photons is a significant determinant in the Monte Carlo simulation. The huge number of photons employed in a single simulation linearly increases the computing time required, but it can reduce the variance in the distribution. The energy is recorded as the number of photons received successfully by the receiver on laser fuze. The paper employs the Monte-Carlo method to generate a statistical distribution from a single point source passing through cloudy medium. The Monte Carlo method is based on two primary optical parameters: scattering coefficient and absorption coefficient.

The weight of the photon lost as its energy is deposited in a scattering event is updated to the Q matrix. Hence, the fraction of light absorbed at each step is affected. Transmission was calculated as the ratio of photons received to the total launched photons.

3.1 The Effect of Scattering and Absorption

Transmission as a function of Scattering

The scattering coefficient μ_{sca} determines the average step size of each photon. The step size, which is related to the typical lifetime of a photon inside the clouds, makes up the majority of the contribution. Higher values of μ_{sca} decrease the average step size and thus increase the number of times a photon is likely to scatter. As expected, low scattering coefficient values result in higher transmission.

Figure 6 shows transmission with absorption coefficient μ_{abs} = 0.3 mm^{-1}. It shows that higher values of μ_{sca} will decrease the average step size and thus increase the number of scattering events. Increasing the scattering coefficient from 1 mm^{-1} to 4 mm^{-1} results in a change to transmission by 30%.

Transmission as a function of Absorption

Absorption coefficient μ_{abs} affects the size of the fraction of light absorbed at each step. It makes up part of the extinction coefficient, along with μ_{sca} as well. Transmission for varying μ_{abs} is shown in Figure 7 Increasing absorption coefficient from 0.1 mm^{-1} to 0.2 mm^{-1} will reduce transmission from 95% to 90%. This implies that variable decoupling can be used during model parameter estimation. Anisotropy variables may be used initially to match a beam profile, while the absorption parameter is individually adjusted to match the corresponding experimentally estimated transmission.

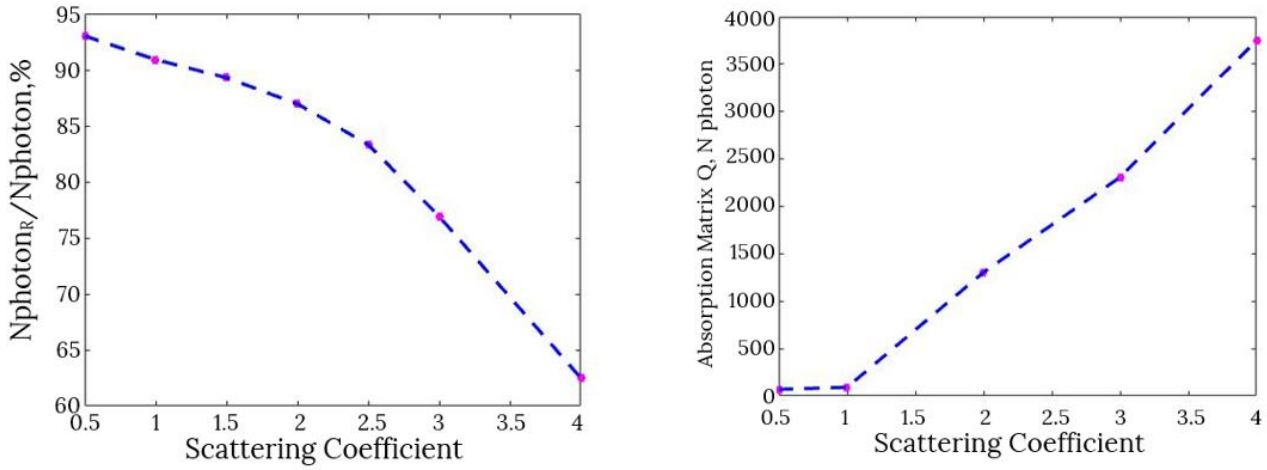

Fig. 6. Transmission as a function of Scattering coefficients

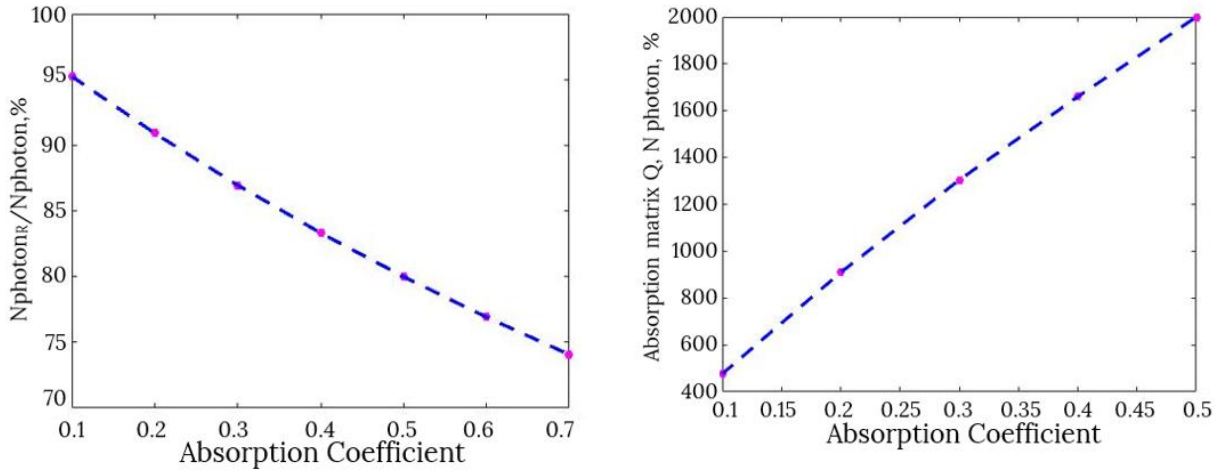

Fig. 7. Transmission as a function of Absorption coefficient

Table 1. A table of atmospheric tranmission factor as a function of visibility for 785 nm, 860 nm and 1550 nm calculated from Equation 3

Visibility (km)	785 nm		860 nm		1550 nm		Weather
	μ_{ext}	T_a	μ_{ext}	T_a	μ_{ext}	T_a	
0.05	78.200	0.2093	78.200	0.2093	78.200	0.2093	
0.2	19.550	0.6764	19.550	0.6764	19.550	0.6764	Fog
0.5	7.8200	0.8552	7.8200	0.8552	7.8200	0.8552	
0.6	6.2889	0.8818	6.2318	0.8828	5.8753	0.8891	
0.7	5.2021	0.9012	5.1080	0.9029	4.5403	0.9132	Mist
0.8	4.3927	0.9159	4.2741	0.9181	3.5817	0.9308	
0.9	3.7682	0.9274	3.6331	0.9299	2.8704	0.9442	
1	3.2728	0.9366	3.1269	0.9394	2.3291	0.9545	
2	1.5459	0.9696	1.4555	0.9713	0.9876	0.9867	Haze
4	0.6898	0.9863	0.6308	0.9875	0.3541	0.9929	
5	0.5213	0.9896	0.4698	0.9906	0.2400	0.9952	

Wavelength Dependence of Atmospheric Attenuation

The extinction coefficient μ_{ext}, which is the sum of two coefficients Absorption coefficient μ_{abs} and Scattering coefficient μ_{sca}

$$\mu_{ext} = \mu_{abs} + \mu_{sca}$$

A better understanding of laser behavior in fog, mist and haze is essential for becoming the preferred solution for selecting the appropriate wavelength to improve the detection capability of the laser fuze. As a result, the paper compares the attenuation of three different wavelengths and six different weather conditions.

The wavelength dependence of atmospheric attenuation in haze is shown in Table 1

However, empirical data for fog show that there is no wavelength dependence for atmospheric attenuation between 785 nm, 860 nm, and 1550 nm. When considering the effects of atmospheric attenuation in fog conditions with visibility less than 500 m, a laser fuze using 1550 nm has no advantage over the others.

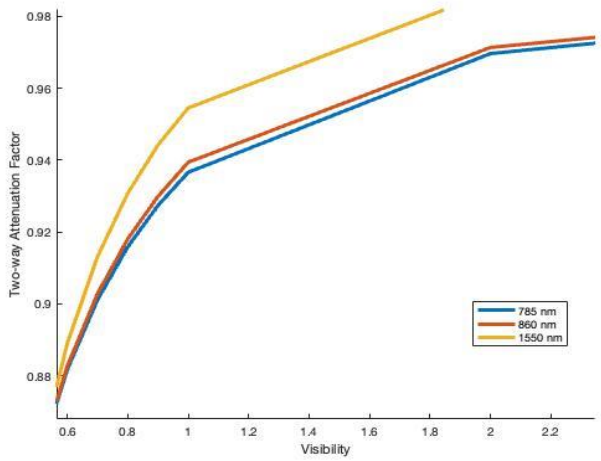

Fig. 8. Squared attenuation factor as a function of visibility

The observation, as shown in Figure 8, is that there is an inherent advantage to using 1550 nm over 780 nm and 860 nm for atmospheric attenuation in mist. If there is a slight increase in haze attenuation, the effect is minor. When there is haze, atmospheric attenuation increases as the wavelength decreases.

The echo signal is primarily composed of the reflected signal from the target, while the proportion of backscattering echo from cloud particles is very small, with a value generally not exceeding 1%. As a result, the target echo differences between laser fuze are caused primarily by differences in target reflection.

4. Conclusions

In this paper, the detection capability of proximity laser fuze in weather conditions is compared in this simulation using three distinct infrared laser wave bands by predicting the effects of laser transmission and atmospheric attenuation factor. The Monte Carlo method is used to construct a detection model that simulates laser echoes in clouds. The method simulates light propagation across various atmospheric attenuation conditions via photon transport by running thousands of photons repeatedly and adding them to a master matrix. When atmospheric attenuation is factored in, there is no advantage to using 1550 nm over 860 nm or 785 nm in fog conditions with visibility less than 500 m. There is a wavelength dependence in hazy conditions (visibility greater than 2 km), and the estimate of less atmospheric attenuation at 1550 nm is most likely correct. This study on wavelength-independent attenuation in various weather scenarios is significant because it can be used to guide and reference the use of wavelength lasers in laser fuze.

Nomenclature

HG : Henyey-Greenstein function

CRediT Author Statement

Hoang Linh Nguyen: Conceptualization, Methodology, Software, Investigation, Validation, Writing-Original Draft. **Trung Dung Pham**: Conceptualization, Methodology, Writing-Review & Editing, Visualization, Supervision. **Hong Son Tran**: Conceptualization, Methodology, Software, Investigation, Validation, Writing-Original Draft. **Thanh Chung Nguyen**: Conceptualization, Methodology, Software, Validation, Writing-Original Draft.

References

A. Welch and M. van Gemert, (1995). Optical-Thermal Response of Laser-Irradiated Tissue, *New York: Springer*.

B. Wilson and G. Adam, (1983). A Monte Carlo model for the absorption and flux distributions of light in tissue, Medical Physics, vol. 10, no. 6, pp. 824-830.

D. M. Winker and L. R. Poole, (1995). Monte-Carlo calculations of cloud returns for ground-based and space-based LIDARS, Appl. Phys. B 60, pp.341–344.

F. Q. Liu, (2017). Quantum cascade lasers: from mid-infrared to THz, *Opt. Optoelectron. Technol.*

H. X. Wang, Y. Z. Zhu, T. Tian, and A. J. Li, (2013). Characteristics of laser transmission in different types of aerosols, *Acta Phys. Sinica* 62, pp. 316– 325.

I.I.Kim,B.McArthur,and E.J.Korevaar, (2001). Comparison of laser beam propagation at 785 nm and 1550 nm in fog and haze for optical wireless communications in Optical Wireless Communications.

K. Sato, K. Yasuo, S. Takushi and S. Isao, (2002). "Laser Welding of plastics transparent to near-infrared rasdiation," in SPIE Proceedings, San Jose.

M. Ilie, J. Kneip, S. Mattei, A. Nichici, C. Roze and T. Girsole, (2007). Laser beam scattering effects in non-absorbent inhomogenous polymers, *Optics and Lasers in Engineering*, vol. 45, no. 3, pp. 405- 412.

M. Kavehrad, B. Hamzeh, (2005) “Beaming Bandwidth via Laser Communications”, 5th Integrated Communications, Navigation and Surveillance Technologies Conference (ICNS), Fairfax, Virginia.

S. Chudamani, J. D. Spinhirne, and A. D. Clarke, (1996). Lidar aerosol backscatter cross sections in the 2-μm near-infrared wavelength region, Appl. Opt. 35, pp. 4812–4819.

S. Prahl, M. Keijzer, S. Jacques and A. Welch, (1989). A Monte Carlo Model of Light Propagation in Tissue, Dosimetry of laser radiation in medicine and biology, no. 5, pp. 102-111.

T. J. Hu, Y. L. Zhao, Y. Zhao, and W. Ren, (2017). Integration design of a MEMS based fuze, *Sens. Actuat.* A 268, pp. 193–200.

V. Kagan, R. Bray and W. Kuhn, (2002) "Laser Transmission Welding of Semi-Crystalline Thermoplastics- -Part 1: Optical Characterization of Nylon Based Plastics," Journal of Reinforced Plastics and Composites, vol. 21, no. 12, pp. 1101-1122.

V. Srivastava, M. A. Jarzembski, and D. A. Bowdle, (1992). Comparison of calculated aerosol backscatter at 9.1- and 2.1-μm wavelengths, *Appl. Opt.* 31, pp. 1904–1906.

W. K. Pratt,(1969). Laser Communication Systems, *J. Wiley & Sons*, New York.

W. Kruse, L. D. McGlauchlin, and R. B. McQuistan, (1962). Elements of Infrared Technology: Generation, Transmission, and Detection, *J. Wiley & Sons, New York.*